Revealing the dynamics of hybrid metal halide perovskite formation via multi-modal *in situ* probes

*Tze-Bin Song, Zhenghao Yuan, Megumi Mori, Faizan Motiwala, Gideon Segev, Eloïse Masquelier, Camelia V. Stan#, Jonathan L. Slack, Nobumichi Tamura, Carolin M. Sutter-Fella**

Dr. T.-B. Song, Z. Yuan, M. Mori, F. Motiwala, Dr. G. Segev, Dr. C. M. S.-F.
Chemical Sciences Division, Lawrence Berkeley National Laboratory, Berkeley, CA 94720, US
E-mail: csutterfella@lbl.gov

Dr. G. Segev, E. Masquelier
Joint Center for Artificial Photosynthesis, Lawrence Berkeley National Laboratory, Berkeley, CA 94720, US

Dr. C. V. Stan, J. L. Slack, Dr. N. Tamura
Advanced Light Source, Lawrence Berkeley National Laboratory, Berkeley, CA 94720, US
present address: National Ignition Facility, Lawrence Livermore National Laboratory, Livermore, CA 94550 US

Keywords: halide perovskites, solution processing, precursor chemistry, multi-modal in situ characterization, annealing time.

The exploration of the synthetic space of halide perovskites hinges on an enormous number of parameters requiring time-consuming experimentation to decouple and optimize. Here, the formation of the prototype metal halide perovskite $CH_3NH_3PbI_3$ ($MAPbI_3$) is investigated at different time and length scales using multi-modal *in situ* measurements to monitor the evolution of crystalline phases, morphology, and photoluminescence as a function of the perovskite lead precursors. Kinetically fast formation of crystalline precursor phases during the spin-coat deposition is observed using PbI_2 or $PbCl_2$ routes. These precursor phases most likely template $MAPbI_3$ film morphology. In particular the emergence of the "needle-like" structure is shown to emerge before film annealing. *In situ* photoluminescence measurements suggest nanoscale nucleation followed by rapid nuclei densification (within a few seconds) and growth. Using this multi-modal *in situ* approach, different formation pathways either via

precursor phases in the PbI_2 and $PbCl_2$ routes or direct perovskite formation from molecular building blocks as observed in the $PbAc_2$ route are identified. Correlation of *in situ* characterization results with photovoltaic device performance demonstrates the power of *in situ* multi-modal techniques, paves the way to a fast screening of synthetic parameters, and ultimately leads to controlled synthetic procedures that yield high efficiency devices.

1. Introduction

Organic-inorganic metal halide perovskites have recently transformed the landscape of light-harvesting solar energy materials while showing promise in a range of other optoelectronic applications. ABX_3 [with A = MA (methylammonium), FA (formamidinium), Cs or other alkali metals; B = Pb, Sn, and X = I, Br, Cl, and alloys thereof] perovskites are easy to synthesize and exhibit superior optoelectronic properties compared to other organic and inorganic semiconductors.[1–7] Typically, halide perovskite thin films are synthesized via a solution process where organic and inorganic precursors are dissolved in organic solvents, then deposited via spin-coating or printing techniques, followed by an annealing step.[8–15] Some of the most frequently used halide perovskite thin film preparation methods to date can be divided into single-step solution deposition and two-step solution deposition. From a practical viewpoint, single-step solution deposition is straightforward, cost-effective, and has fewer control factors as compared to the solution engineering approach with antisolvent dripping.[16,17] Therefore, many efforts to achieve high quality halide perovskite thin films from one-step solution deposition have been reported in recent years.[18–20] The processing window for high performance devices, however, is narrow due to an increasing number of experimental parameters which require time-consuming efforts for optimization to yield reproducible film quality and high device performance.[21,22] In this regard, *in situ* techniques play a critical role in providing time-resolved information on the evolution of halide perovskites under various synthetic conditions. Recent reported *in situ* studies making use of diffraction measurements,[23–31] terahertz spectroscopy,[32] Fourier transform infrared spectroscopy,[23] UV-Vis spectroscopy,[27] simultaneous X-ray scattering and device

performance,[33] transmission electron microscopy,[34] and spectrally ambiguous photoluminescence (PL) correlated with *ex situ* device performance[35] gradually shed light on halide perovskite formation and its evolving material properties as well as on device performance. Despite these advancements, critical insights on phase formation and evolution of film properties occurring during spin-coating and immediately after deposition go unobserved during the ~2-5 min wet film transfer time prior to commencing subsequent *in situ* studies. While the perovskite field moves towards chemically more and more complex compositions, the influence of the precursor chemistry on the evolving material properties remains ambiguous.[26,30,36] Hence, a better understanding of halide perovskite formation is extremely important to achieving directed synthesis and control over perovskite film quality and device performance. Here, we investigate the formation of $CH_3NH_3PbI_3$ ($MAPbI_3$) prepared from different lead precursors (PbI_2, $PbAc_2$, $PbCl_2$) using one-step solution deposition. In order to avoid convoluted effects from complex precursor chemistries we chose to investigate the prototype $MAPbI_3$, which is often used for fundamental studies.[37,38] The three different lead precursors have been chosen because those are currently employed to synthesize high quality films in order to investigate their role in film formation and evolution of optical and structural properties.[21,39,40] We find kinetically fast formation of crystalline precursor phases using Pb-halide precursors. These precursor phases form already during spin-coating and probably template final $MAPbI_3$ film morphology. This is presumably one of the first times that crystallization properties are characterized during spin-coat deposition. Particularly the “needle-like” morphology found when employing the PbI_2 precursor emerges before film annealing. *In situ* PL is used to investigate nucleation and growth and suggests nanoscale nucleation followed by nuclei densification within a few seconds. Using $PbAc_2$ as the Pb precursor leads direct growth of perovskite phase from molecular building blocks. Results from *in situ* measurements can be correlated to perovskite photovoltaic performance

and explain for example the need for longer annealing times when using $PbCl_2$ instead of PbI_2 or $PbAc_2$. In order to reveal the formation mechanisms of halide perovskite thin films, during and right after spin-coating, we designed and developed two state-of-the-art multi-modal *in situ* characterization platforms using synchrotron X-ray diffraction in one setup, and photoluminescence, and optical microscopy in a second lab-based system. Thereby, we mimic the typical synthetic process and unravel the very early stages (initial seconds) of halide perovskite formation - including processes happening during the spin-coat deposition. Ultimately, the correlation of *in situ* characterization results with photovoltaic device metrics demonstrate the power of *in situ* multi-modal techniques as promising tools to optimize synthesis parameters and thus, device performance.

2. Results

2.1 *In situ* synchrotron X-ray diffraction

Perovskite precursors were prepared using MAI:X (X = PbI_2, $PbAc_2$, $PbCl_2$) ratios of 1:1, 3:1, and 3:1, with N,N-dimethylformamide (DMF) as the solvent. They were deposited on glass substrates using a one-step spin-coating process in an ambient environment followed by annealing at 110 ºC (details described in the experimental sections). According to literature, there is no evidence of acetate or chlorine being incorporated into the film in large amounts thus, we refer to the formation of $MAPbI_3$ in each Pb route.[26,27,43] First, to establish unambiguous structure-property relationships, we designed and integrated an *in situ* diffraction characterization system with a remotely controlled spin coater and heating capability at beamline 12.3.2 of the Advanced Light Source. Integrating a spin coater in the synchrotron hutch allowed us to record the phase evolution during the spin-coating process (spin-coating is used by the vast majority of research groups for the formation of halide

perovskite films) and thus, provided a better understanding of the perovskite phase formation. Additionally, we investigated the phase transformation of perovskite precursors immediately after spin-coating to capture the fast perovskite formation processes during the first seconds without having sample transfer processes, as mentioned in the introduction section. With this state-of-the-art system, we are able to further investigate the structural properties of the thin films prepared using the PbI_2, $PbAc_2$ and $PbCl_2$ routes.

In **Figure 1a**, we show the *in situ* diffraction patterns of the perovskite thin film prepared from PbI_2 route within 1 min of annealing. During the first 11 s of annealing, there is no perovskite phase but diffraction peaks labeled P1 include two low-angle peaks at 2θ = ~8.1° and ~9.5°. Those peaks are generally assigned to precursor phases, but it is hard to confirm the structure by *ex situ* characterization due to their instability. With our system, we are able to identify the precursor phase as the orthorhombic $(MA)_2(DMF)_2Pb_3I_8$ phase. We suggest that formation of the $(MA)_2(DMF)_2Pb_3I_8$ precursor phase is the reason for the formation of the needle-like morphology observed in the optical images (**section 2.2**). To confirm this hypothesis, we show the 2D diffraction pattern as well as the converted diffraction pattern of the film during the spin-coating process (i.e. before annealing) in **Figures S1a**, **S2a+d,** and **S3a**. There is a slight difference in preferential orientation of our $(MA)_2(DMF)_2Pb_3I_8$ phase compared to Petrov et al.[41] but this is plausible given that P1 is a PbI_2-rich precursor phase and that PbI_2 does show different orientations depending on whether it crystallizes rapidly or slowly.[42] The 2D diffraction patterns of the P1 phase (Figure 1a) do show preferential orientation which would induce the integrated intensity in the 1D patterns to deviate from peak intensity distributions of reference or calculated patterns. It is clear that the $(MA)_2(DMF)_2Pb_3I_8$ phase is the only phase present, thus leading to the needle-like morphology. This finding is in agreement with Petrov et al.[41] After about 10 s the final

annealing temperature of 110 °C is reached, and the $MAPbI_3$ phase starts to be observed after ~12 s. The $(MA)_2(DMF)_2Pb_3I_8$ phase gradually disappears after ~20 s of annealing, and the perovskite phase becomes the only phase present in the film until the PbI_2 phase appears at ~ 5 min annealing as shown in **Figures 1a** and **S1a**. Formation of the PbI_2 phase (apparent by a diffraction peak appearing at $2\theta \sim 12.7°$) during annealing indicates $MAPbI_3$ decomposition due to evaporation of MAI.[23]

In the $PbAc_2$ route, surprisingly, we observed the direct emergence of perovskite phase after ~12 s of annealing (**Figures 1b**, **S2b+e,** and **S3b**), without any crystalline precursors. This differs from previous reports where unidentified precursor phases were found.[26] A possible reason for this discrepancy could be that our system does not require a wet film transferring time and thus, no unwanted chemical reactions with the environment might occur leading to different crystallization pathways as compared to literature. The measurement conditions used here better represent synthesis conditions in the laboratory and thus, are considered closer to the actual crystallization pathway. Additionally, these diffraction results support the observation made by optical imaging (**section 2.2**) where no crystalline features were found during the first few seconds of annealing. The correlation between the optical image and the diffraction provides strong evidence that there is no observable precursor phase in the $PbAc_2$ route under our experimental condition. The PbI_2 phase as a decomposition product appears after ~90 s of annealing, earlier than using the other two routes, implying that the prolonged annealing is not favorable in the $PbAc_2$ approach.

When using the $PbCl_2$ route, crystallization kinetics are very different compared to the other two routes, as illustrated in **Figures 1c** and **S1c**. Although, Cl^- is not incorporated into the crystal lattice in substantial amounts[27,43,44] it influences the crystallization pathway and retards $MAPbI_3$ formation. There is a different precursor phase (labelled as P2) present, and

perovskite phase is co-present with P2 during the annealing process in the early formation step. Interestingly, the diffraction peaks of the perovskite and P2 phases both appeared at the end of spin-coating process i.e. before annealing (**Figure S3c**), and then P2 phase becomes dominant within the first 400 s annealing. After ~350 s annealing, the intensities of the perovskite peaks gradually become stronger and, after ~1200 s annealing, the perovskite phase becomes the dominant phase in the film with a small quantity of PbI_2 phase present. It is worth noting that the initial strong signal at $2\theta =$ ~28.3° [which coincides with the (200) perovskite peak] might be related to the P2 phase. Presence of incomplete diffraction rings (Figure S1c) indicate that the perovskite crystalline domains are oriented, which is different than in the PbI_2 and $PbAc_2$ routes. The latter two show complete rings and therefore randomly oriented crystalline domains. This observation is in alignment with the fast $MAPbI_3$ formation in the PbI_2 and $PbAc_2$ routes and very slow $MAPbI_3$ formation in the $PbCl_2$ route. Oriented growth in the presence of Cl has been reported before and was explained by a minimization of the Gibbs free energy, including the surface and interface energy, thus promoting preferential growth of specific crystallographic orientation.[45] Besides a difference in preferential orientation, $MAPbI_3$ synthesized from a $PbCl_2$ precursor shows the same characteristic peaks, and therefore has an identical lattice as $MAPbI_3$ synthesized via the PbI_2 route.[43] In the work by Yu et al., it was stated that the formation of $MAPbI_3$ using the $PbCl_2$ route is probably driven by the gaseous release of Cl-containing organic products such as CH_3NH_3Cl.[43] Furthermore, the authors discussed that the retarded perovskite formation is likely related to a $CH_3NH_3^+$-rich environment.[43] Considering that both the $PbCl_2$ and $PbAc_2$ routes start with a $CH_3NH_3^+$-rich environment but $MAPbI_3$ forms within ~12 s in the $PbAc_2$ route, we believe that Cl plays a significant role in forming a kinetically fast and thermodynamically stable precursor phase. Yu et al. proposed the formation of $(CH_3NH_3)_{x+y}PbI_{2+x}Cl_y$ as an intermediate

precursor phase in the $PbCl_2$ route before excess Cl leaves the film via gaseous CH_3NH_3Cl[43] however, peak overlap and textured diffraction patterns (**Figure S1c**) make it difficult to identify the structure of the P2 phase (full 30 min diffraction heat maps are provided in **Figure S4**).

2.2 *In situ* imaging

The morphology of perovskite thin films is an important factor in achieving high performance devices. To study the relationship between chemical precursors and film morphology during annealing, we integrated optical microscopy to record *in situ* images as shown in **Figure 2** and **Figures S5-7.** The very right column in **Figure 2** shows the corresponding SEM images of perovskite films annealed for 30 min to give a sense of the morphology at higher magnification. Please note that the experimental conditions are different in **sections 2.2** and **2.3** compared to **section 2.1** because in 2.1, spin-coating and heating was taking place on the same puck while in 2.2 and 2.3 experiments were performed in a typical configuration of using a spin coater next to a hot plate. This implies that in the latter case the hot plate is already at the final temperature, 110 °C, while, in the synchrotron hutch, the puck is heating up directly after the spin-coating is terminated. These different experimental configurations induce a ~5-10 s offset in terms of heating the sample to the final temperature. In the PbI_2 route (**Figure 2a** and **Figure S5**), the typical needle-like morphology is immediately observed after the spin-coating process and remains unchanged during the total annealing time of 30 min. This needle-like morphology is related to the initially forming precursor phase P1 as discussed previously. The needle-like morphology was not observed in the other two chemical routes as shown in **Figures 2b, c**. In the $PbAc_2$ route (**Figure 2b** and **Figure S6**), we note that there are no observable crystal/grain features right after the spin-coating process. Within 2-3 s of annealing, distinct nucleation spots are present leading to a

fine and fully covering film after prolonged annealing. Finally, in the $PbCl_2$ route (**Figure 2c** and **Figure S7**), we can observe some crystal/grain features immediately after the spin-coating process, and relatively larger features compared to the ones in the $PbAc_2$ route can clearly be seen. These morphologies remain nearly unchanged after the first 3 s of annealing for all three precursor routes. When comparing the microscopy images during the early stage of film formation, it appears that the number of particles/crystals is significantly higher in the case of the $PbAc_2$ route than in the $PbCl_2$ route. It takes only 1-2 s for separated particles/crystals to form a fully covered film in the $PbAc_2$ route, which is slightly faster than ~3 s in the $PbCl_2$ route. These results confirm previous literature reports, where faster film formation and smaller crystal sizes have been obtained using $PbAc_2$ instead of PbI_2 or $PbCl_2$, with $PbCl_2$ forming the largest crystals.[26] The series of *in situ* optical microscopy images strongly suggests that the Pb-route directly influences the film morphology and shows that the morphology is defined in the very early stage of the formation, either during spin-coating or during the first few seconds of annealing. These results also support the need to control perovskite thin film morphology in the PbI_2 route using antisolvent dripping during the one-step spin-coating process to prevent needle-like morphology formation.[46,47]

2.3 *In situ* photoluminescence

To provide complementary information to the optical imaging and crystallographic properties *in situ* PL measurements were performed to probe luminescence characteristics during $MAPbI_3$ formation and annealing. It is known that $MAPbI_3$ exhibits strong PL response due to its direct bandgap properties and high defect tolerance[48–50], therefore PL spectroscopy provides a great opportunity to track the optical response from evolving $MAPbI_3$ films. Moreover, given the high brightness of halide perovskites, the response of PL

spectroscopy can be acquired with a sub-second timescale, enabling the investigation of the fast reactions during the formation processes.

In **Figure 3**, we show the time evolution of the PL signals during $MAPbI_3$ film formation from the three perovskite precursors. PL intensity and spectral position of the PL peak were obtained from Gaussian fitting to the spectrally resolved PL data. During the spin-coating process there is no PL response (**Figure S8**), but PL emission immediately appeared while annealing for 1-2 s in all three routes. Full 30 min PL emission maps as well as representative PL spectra are also provided in **Figure S9**.

Interestingly, the early PL emissions in all routes investigated appeared at higher energies ~1.78 eV in PbI_2, ~1.66 eV in $PbAc_2$, and ~1.77 eV in $PbCl_2$, and then red-shifted to lower energy ~1.63 eV, the typically reported PL emission energy of $MAPbI_3$ ($MAPbI_3$ is in cubic phase at the annealing temperature of 110 °C).[51] Both Pb halide routes (PbI_2 and $PbCl_2$) exhibit significant differences between initial and final PL emission energy (ΔE, illustrated by the height of the shaded areas in Figure 3a, c, e) of 150 and 140 meV respectively, while ΔE = 30 meV in the $PbAc_2$ route. Thus, we observe that the non-halide Pb source has the least impact on ΔE. Red-shifting is related to crystal growth with larger shifts indicating smaller initial crystal size.[52,53] The energy of the spectral maximum can be interpreted as the bandgap of the sample in first approximation.[54,55] A correlation between spectral PL position and crystal size has been shown previously.[56] In this study by Nie et al., a red-shift of ΔE ~ 25 meV was reported for a grain size change by a factor of 20, from 20 to 400 μm^2.[56] In this study, in the Pb halide routes, ΔE = 140-150 meV, which indicates a significantly larger change from nuclei size to grain size. Although the chemistry used for the synthesis of 3D $MAPbI_3$ films is different than that for the synthesis of nanocrystals (typically no surface ligands are used for the synthesis of thin films), we propose that nucleation starts on the nm-

scale (or sub-micrometer scale), similar to the initial stages of nanocrystal growth.[57,58] In the latter, ligands would terminate the growth of nanocrystals and therefore dominate spectral PL emission (size effect), while in thin films PL emission is related to the bandgap. A nano-assembly model via formation of PbI_6^{4-} cage nanoparticles has been suggested before as a growth model for $MAPbI_3$ films.[23] ΔE in the acetate route is comparatively small and could indicate larger nuclei as compared to the I- and Cl-routes. In addition, it can be seen that Δt, the time it takes for high to low energy shift, is the shortest in the $PbAc_2$ route. This observation is similar to the finding from *ex situ* X-ray diffraction results where $MAPbI_3$ formation from $PbAc_2$ route was determined to be faster than from the other Pb salts.[26] The shift of PL emission in the $PbCl_2$ route is significantly retarded in comparison to that of the PbI_2 or $PbAc_2$ routes. It takes ~20 min of annealing to reach the stable PL energy of ~1.63 eV, with complete PL signal disappearance for ~5 min as shown in **Figure 3e**. Moreover, the PL peak energy change between 300-1800s following first a reduction in energy and second a slight increase in emission energy (**Figure 3e**) might indicate an interplay between the halides I and Cl in the following way: A small amount of initially incorporated Cl in $MAPbI_3$ (resulting in higher energy emission peak position) could slowly leave the perovskite film as evidenced by a drop of PL peak energy. However, in parallel a second mechanism that is, decomposition of P2, could release Cl which to some extend gets incorporated in the $MAPbI_3$ film. These subtle compositional variations have not been observed in the diffraction measurements. The reason for that could be the thermal expansion of the Cu puck used in the synchrotron hutch which leads to a sample increase over time resulting in a peak position shift towards higher 2θ values. Next, we turn our attention to the PL intensity change, which exhibits two maxima over time. Temporally, we consider two effects to contribute to the change of PL intensity. The first effect is nucleation and increasing nucleation density, while

the second effect is crystal growth. We propose that the initial very fast PL intensity increase followed by an intensity drop we propose that this is related to the ΔE change, implying an initial fast nucleation of perovskite crystals. This fast nucleation is triggered by supersaturation upon solvent evaporation, and the initial PL intensity rise stems from an increase in perovskite amount due to an increase in nucleation density. Later, when PL emission is not dominated by nuclei sizes anymore but reflects the bandgap of the $MAPbI_3$ material (~1.63 eV), PL intensity again rises due to crystal growth. After the second intensity maximum, the PL intensity gradually drops by up to about two orders of magnitude probably due to photodarkening and thermally induced effects. The *in situ* PL data is not corrected for absorption but compared here in relative intensities, therefore, *ex situ* 100-T%-R% of samples annealed for 15 and 30 min is provided in **Figure S10a+b**. In addition, to deconvolute combined thermal and photo-effects *ex situ* PL spectra and the PL peak intensity plotted over time, both taken at room temperature, are shown in **Figure S10c+d**. Over time the PL peak intensity is increasing for all Pb-routes (only a slight PL rise was observed in the PbI_2 route and a rise by 6 and 2.5 times in the $PbAc_2$ and $PbCl_2$ routes, respectively). This increase has been assigned previously to a so-called oxygen healing via the formation of a superoxide O_2^- which fills in iodide vacancies resulting in a PL intensity increase.[37,59,60] The comparison of PL evolution at room temperature versus at 110 °C indicates that thermal effects in oxygen and humidity containing atmosphere prevail and significantly quench the PL signal. However, this comparison is between $MAPbI_3$ in tetragonal phase (at room temperature) versus in higher symmetric cubic phase (at 110 °C) which might play a role with respect to stability under different stimuli.

In addition, the full width at half maxima (FWHM) are evaluated for the three different Pb-routes (**Figure 3g**). Generally, the FWHM drops initially and stabilizes until it starts to

increase towards longer annealing times. Interestingly, the Pb-halide routes show a significantly higher FWHM in the beginning compared to the $PbAc_2$ route which might be correlated to the larger ΔE observed for PbI_2 and $PbCl_2$ related to the nm-scale nucleation discussed above. The FWHM reaches a minimum in each Pb-route that is on the time-scale close to the appearance of PbI_2 phase as a consequence of $MAPbI_3$ decomposition (indicated by the time in Figure 3g). Thus, the evolution of the FWHM from initial nucleation to the onset of decomposition can be interpreted as grain growth and phase formation. With the beginning of decomposition around ~300s, 90s, and 1200s in the PbI_2, $PbAc_2$, and $PbCl_2$ routes, respectively, the FWHM increases indicating decreased material band inhomogeneity possibly caused by recombination at $MAPbI_3/PbI_2$ boundaries. Given the insights discussed above, *in situ* PL represents a powerful way of monitoring nucleation, growth and decomposition of halide perovskites.

To examine potential light-induced effects in the film formation from the laser probe, we varied the laser power illumination density between 6 - 30 mW/cm^2 (compare **Figures S11-13**). The illumination power density does not significantly influence ΔE. The main difference is the increase in overall signal intensity with increasing illumination, as expected. There might be an effect on the kinetics, particularly in the $PbCl_2$ route (**Figure S13**), where the first and second PL features appear ~1 s and ~100 s earlier at 30 mW/cm^2 compared to the measurement performed at 6 mW/cm^2. Yet, the highest PL intensity still appears in the same time frame (~800 s). Currently, the influence of light during synthesis is not fully understood in the perovskite community;[61,62] we believe that *in situ* PL could be a promising platform to further examine the light effects on perovskite formation.

3. Discussion

We summarize results obtained from multi-modal *in situ* measurements as a function of the Pb route in **Figure 4**. In the PbI_2 route (**Figure 4a**), needle-like morphological features captured by optical microscope imaging during the film formation process and confirmed by synchrotron diffraction are related to the precursor phase P1 [$(MA)_2(DMF)_2Pb_3I_8$]. Being capable of spin-coating inside the synchrotron hutch revealed that P1 forms already during the dynamic wet film spinning process. Since the morphology is maintained until the end of crystallization while the crystal phase transforms from P1 to perovskite, we conclude that P1 determines film morphology, and that the perovskite phase nucleates and grows while converting P1 within the pre-defined morphology. Moreover, based on the direct comparison of *in situ* PL and *in situ* diffraction results, it is highly likely that the high energy PL emission at 1.78 eV and sequential red-shifting observed in the PbI_2 route is related to nucleation on the sub-micrometer scale and growth of the perovskite phase, since there is no PL signal observed during the spin-coating step or at 0-1 s annealing when the P1 phase was the only phase present. This relationship is supported by the very similar perovskite phase formation rate from *in situ* diffraction results where the perovskite phase appears at ~2 s annealing and becomes the only phase at ~10 s annealing (note: there is a ~10 s delay for raising the temperature to 110 °C in the diffraction system).

In contrast, using the $PbAc_2$ route does not result in crystalline precursor phases nor features during the spin-coating step, as confirmed by all three *in situ* characterization methods. Direct perovskite phase formation and growth from molecular building blocks occurred and was completed within the first 5 s of annealing. We observe high density nucleation and fast growth from the *in situ* optical imaging, which typically leads to a fully covered thin film with small domain sizes as confirmed by the SEM image shown in **Figure 2b**. One reason for this

fast formation process is probably the fact that MAAc is thermally unstable and decomposes much earlier than MAI or MACl.[26] Therefore, formation of perovskite phase from $PbAc_2$ route is faster than with the other precursor routes, as characterized from *in situ* diffraction. From the *in situ* PL spectra, it was observed that the red-shift of PL emission from high (~1.66 eV) to low energy (~ 1.63 eV) only takes 3-4 seconds, which corresponds to a similar timestamp of phase formation (from *in situ* diffraction) as well as to the completion of film formation. Additionally, it is noted that the initial PL emission energy detected in the $PbAc_2$ route is lower than in the other two routes. It is unclear at the moment if this means larger initial nuclei size, or if we were not able to capture a very fast nucleation and growth process. Although the $PbAc_2$ route provides a faster perovskite formation pathway, we would like to point out that the PbI_2 phase also appeared much earlier than in the other two routes which could indicate a stability concern using this route.[63]

In the $PbCl_2$ route, it was found that the precursor phase P2 and the perovskite phase both form during the spin-coating process, and that P2 becomes dominant within the first 20 min of annealing. Weak diffraction signals from perovskite phase can be observed after ~ 400 s of annealing and become increasingly intensive. The early formation of the perovskite and P2 phases is evidenced by the crystalline features observed by *in situ* optical imaging. Moreover, the *in situ* PL emission spectra shows high-energy emission (~ 1.77 eV) in the first 10 s of annealing with weak PL intensity that can be attributed to the small amount of perovskite phase with quantum-confined nucleation. No PL signal was observed between 10 and 300 s of annealing. Possibly, the PL signals are too weak to be detected by our set-up due to a combination of a small amount of perovskite phase being present and thermal quenching. While the amount of perovskite phase increases after ~350 s of annealing, the PL emission simultaneously re-appeared and the PL spectra red-shifted toward ~ 1.63 eV. These results

show that the formation of the P2 phase is more kinetically favorable than of the perovskite phase. The P2 phase is probably related to the release of gaseous Cl-containing precursor phases (such as MACl[43]) delaying the formation of $MAPbI_3$ phase. After prolonged annealing, the P2 phase gradually diminished and the perovskite phase grew, with a small amount of PbI_2 phase co-present. Under our experimental conditions, we do not observe a single-phase window in the $PbCl_2$ route. Although pure phases can't be achieved from this route, it is reported that the excess PbI_2 could be beneficial to passivate grain boundary defects and improve the device performances.[64,65] Therefore, a longer thermal annealing is required in the $PbCl_2$ route to prevent the residuals of P2 phase.

The discussed formation paths are determined by the solution chemistries and are independent of substrate conditions. This is confirm by experiments on SnO_2/FTO substrates shown in the supporting information (**Figure S14-15**).

Finally, we prepared a series of devices from these three different precursor routes after various annealing times as summarized in the supporting information **Figure S16**. As expected, the perovskite devices following the PbI_2 route result in poor device performances after 10, 30, and 300 s of annealing, with low short circuit currents (J_{sc}) of about 11-12 mA/cm^2 caused by the overall poor absorption (< 50%), low fill factors (FF) between 31-34% and poor open circuit voltage (V_{oc}) due to poorly covering morphology as observed by *in situ* imaging . In comparison, the perovskite devices from the $PbAc_2$ route performed better and showed the best performance (efficiency > 8%) after short annealing times (10 and 30 s) followed by a drop in performance, mostly due to a reduced FF which drops by about 10% from above 50% to 43% when annealed for 300 s. This finding is in line with what was discussed before, that the $PbAc_2$ route results in high film coverage and ultrafast perovskite phase formation but also in early formation of the PbI_2 phase (*in situ* diffraction), which could

lead to a drop in J_{sc} and FF. Excess co-presence of PbI_2 has been shown to deteriorate device performance, possibly due to the blocking of the electron transport.[64] Because the perovskite formation in the $PbCl_2$ route is significantly slower than in the other two routes, we are not able to obtain a functional device after short annealing times (< 1800 s). After prolonged annealing, devices with performance of up to 10% were achieved, higher than in the other two routes. Typically, slow crystal growth leads to better crystal quality, as confirmed by the superior photovoltaic parameters when following the $PbCl_2$ route. As seen by the *in situ* characterizations (diffraction and PL), the long-time annealing is required for the $PbCl_2$ route in order to convert the P2 to perovskite phase and remove of excess Cl. Note for all Pb-routes, that device performances are low compared to state-of-the-art devices due to the absence of any solution engineering strategies or advanced compositional absorber tuning.

4. Conclusion

The development of complementary multi-modal *in situ* characterization tools enabled us to reveal the detail formation pathways of spin coated $MAPbI_3$ films prepared by PbI_2, $PbAc_2$ and $PbCl_2$ routes. We successfully scrutinized the evolution of perovskite thin films and established links between *in situ* diffraction, imaging, photoluminescence, and photovoltaic performance to provide new insights into factors that govern halide perovskite formation and properties. We find that 1) in the Pb halide routes, crystalline precursor phases form already during spin-coat deposition before annealing, while perovskite phase forms directly from molecular building blocks in the $PbAc_2$ route; 2) perovskite film morphology develops likely during the spin-coating process in the PbI_2 and $PbCl_2$ routes and is templated by the crystalline precursor phases, or in the first seconds of annealing in the $PbAc_2$ route; with the "needle-like" morphology determined by formation of $(MA)_2(DMF)_2Pb_3I_8$ as precursor phase in the PbI_2 route; 3) *in situ* PL during annealing suggests nanoscale nucleation, densification,

and growth in the Pb halide routes and thus can be a valuable monitoring tool; and 4) the results obtained from *in situ* measurements can help to design experimental parameters to enhance photovoltaic performance and stability. For example, adjusting the annealing duration is incremental to obtain pure perovskite phase samples without precursor phases and before decomposition accompanied by PbI_2 formation. As a second example, correlating the precursor chemistry with the formation of a poorly covering morphology can indicate that intervention in the crystallization pathway, for example by antisolvent dripping during spin-coating, can provide a means to engineer film morphology by suppressing precursor phase formation. The presented complimentary suite of *in situ* tools will be greatly beneficial to halide perovskite synthesis, enabling the systematic scanning of a wide parameter space without the need for synthesizing full devices or for in-line quality control. The developed platform will be applied to investigating polyelemental perovskite semiconductors[66] in future studies, and the insights provided here will pave the way to develop design rules for commercially relevant high efficiency devices.

Experimental Section

Film fabrication. Methylammonium iodide (CH_3NH_3I, MAI) (Greatcell Solar, CAS No. 14965-49-2), lead chloride ($PbCl_2$, 99.999%), lead acetate trihydrate ($PbAc_2$, 99.999%), and anhydrous N,N-dimethylformamide (DMF, 99.8%) were purchased from Sigma-Aldrich. Lead iodide (PbI_2, 99.9985%) and tin oxide (SnO_2, 15% in H_2O) nanoparticle dispersion were purchased from Alfa Aesar. Chemicals were used as received. The precursor solutions were prepared following the originally most frequently used preparation recipes. We used molar ratios of MAI to 0.6 M PbX_2 (X = I, Ac, Cl) of 1:1 (MAI 95.4 mg : PbI_2 276.6 mg), 3:1 (MAI 286.2 mg : $PbAc_2$ 227.6 mg), and 3:1 (MAI 286.2 mg : $PbCl_2$ 166.9 mg), respectively. All

precursors were dissolved in DMF (1 mL). $MAPbI_3$ films were prepared by a one-step spin-coating process at 500 rpm for 5 s, followed by 2,000 rpm for 30 s. After spin-coating, the films were annealed at 110 °C on a hotplate in the fume hood or glovebox for 30 min.

Combined in situ measurements. To be able to study the formation of perovskites optically as well as structurally on the same time axis, we designed two different setups. The first allowed direct monitoring of photoluminescence (PL) emission and optical microscopy during synthesis. The second allowed spin-coating and film drying under lab conditions but in the synchrotron hutch for diffraction measurements.

In situ PL. PL measurements were acquired on a home built confocal setup using a 532 nm laser diode, a plano-convex lens above the substrate, a 550 nm long-pass filter and a fiber coupled Ocean Optics spectrometer (Flame) calibrated by the manufacturer. The distance between the plano-convex lens and the substrate was optimized such that the PL intensity of a dry film was maximized. The working distance was not adjusted with the change of the wet film thickness during the drying process. A maximum power density of ~30 mW/cm^2 was used during *in situ* PL measurements on glass substrates. A maximum power density of ~300 mW/cm^2 was used during *in situ* PL measurements on FTO/SnO_2 substrates. PL emission signals were fitted using single Gaussian peak fitting after linear background removal, $R^2 > 0.998$. The intensity plotted in Figure 3 corresponds to the peak intensity.

In-situ optical imaging. Optical images were acquired using a home build microscope set-up equipped with a Thorlabs CMOS camera (DCC3240C) and a Thorlabs white light LED source (MCWHL5). After spin-coating, the samples were transferred immediately onto the pre-heated stage at 110 °C under immediate recording.

In-situ synchrotron X-ray diffraction. Synchrotron diffraction measurements with an incident angle of 2° were conducted at beamline 12.3.2 at the Advanced Light Source, Lawrence Berkeley National Laboratory. The detector (DECTRIS Pilatus 1 M) was located at 40° with respect to the direct beam and approximately 164 mm from the sample. The detector geometry was calibrated using a finely ground Al_2O_3 reference sample. Measurements were performed at 8 keV (1.54982 Å), with an estimated flux of ~$6x10^8$ photons/s on an exposed area of about 3 mm^2 (10 mm x 0.3 mm) for a total of 30 min. In order to avoid transfer times of wet precursor films, we designed and installed a spin coater in the synchrotron hutch connected to a remotely triggered resistive heater. After dropping the perovskite precursor solution, films were spin-coated using the same program as under lab conditions. After spin-coating, the sample was immediately heated on average at ~6 °C /s to 110 °C. It is noted that the annealing time of the diffraction data is slightly retarded (~5-10 s) in comparison to PL and optical microscopy due to the slower heating rate imposed by the resistive heating capacity of the spin coater at the synchrotron end station. The typical frame rate for diffraction data collection was 0.5 frames/s (2 frames/s did not result in additional information). The 2D diffraction images were processed using the X-ray microdiffraction analysis software (XMAS).[67] Importantly, sample damage was not observed under the experimental conditions described, which would either manifest as presence of PbI_2 phase and/or visible bleaching of the sample where it is exposed to the photon irradiation.

Other Material Characterizations. A field emission scanning electron microscopy (SEM, Quanta FEG 250, FEI) was used to acquire SEM images. An electron beam acceleration of 5 kV was used.

Device processing and characterization. First, ITO coated glasses were cleaned with detergent, deionized water, acetone, and isopropanol to serve as the bottom electrode. Next,

the ITO substrates were treated with UV-Ozone for 10 min before deposition of a thin layer of SnO_2 according to previous reports.[65] After that, 1 M of perovskite precursors (MAI:PbI_2 (159 mg : 461 mg); 3MAI:$PbAc_2$ (477 mg : 379.3 mg); 3MAI:$PbCl_2$ (477 mg : 278 mg)) dissolved in DMF (1 mL) was spin coated onto SnO_2 at 2000 rpm for 30 s, and then annealed at 110 °C for different time periods. 2,2,7,7-tetrakis(N,N-dip-methoxyphenylamine)-9,9-spirobifluorene (Spiro-OMeTAD) was used as the hole transporting layer (HTL) and was deposited on top of the perovskite layer using spin-coating at 3000 rpm for 30 s. The solution consisted of 72.3 mg Spiro-OMeTAD, 35 µl bis(trifluoromethane) sulfonamide lithium salt (Li-TFSI) stock solution (260 mg Li-TFSI in 1 ml acetonitrile), 30 µl 4-tertbutylpyridine, and 1 ml chlorobenzene. An 80 nm thick Au film was thermally evaporated as a top electrode using a shadow mask, with device effective area of 0.108 cm^2. The photovoltaic characteristics were obtained using a Keithley 2400 Source Meter under simulated 1-sun AM 1.5G illumination (100 mW/cm^2), calibrated by using a KG-5 Si diode. The J–V measurements were carried out in ambient air and the devices were measured in reverse scan (1.2 V to 0 V).

Supporting Information
Supporting Information is available from the Wiley Online Library or from the author.

Acknowledgements
This manuscript was prepared with support from the Laboratory Directed Research and Development (LDRD) program of Lawrence Berkeley National Laboratory under U.S. Department of Energy contract number DE-AC02-05CH11231 (T.-B.S. and C.M.S.-F.) and under the auspices of the U.S. Department of Energy by Lawrence Livermore National Laboratory under Contract DE-AC52-07NA27344 (CVS). This research used beamline 12.3.2 at the Advanced Light Source, which is a DOE Office of Science User Facility under contract no. DE-AC02-05CH11231. Help with device synthesis from Jingbi You group is gratefully acknowledged. Constructive feedback during writing of the manuscript provided by Matt Jurow is highly appreciated.

Received: ((will be filled in by the editorial staff))
Revised: ((will be filled in by the editorial staff))
Published online: ((will be filled in by the editorial staff))

References

[1] J. Xue, J.-W. Lee, Z. Dai, R. Wang, S. Nuryyeva, M. E. Liao, S.-Y. Chang, L. Meng, D. Meng, P. Sun, O. Lin, M. S. Goorsky, Y. Yang, *Joule* **2018**, *2*, 1866.

[2] M. Grätzel, "The light and shade of perovskite solar cells," DOI 10.1038/nmat4065can be found under https://www.nature.com/articles/nmat4065, **2014**.

[3] S. D. Stranks, H. J. Snaith, *Nat Nano* **2015**, *10*, 391.

[4] L. M. Herz, *ACS Energy Lett.* **2017**, *2*, 1539.

[5] C. C. Stoumpos, M. G. Kanatzidis, *Advanced Materials* **2016**, *28*, 5778.

[6] M. A. Green, Y. Jiang, A. M. Soufiani, A. Ho-Baillie, *J. Phys. Chem. Lett.* **2015**, *6*, 4774.

[7] G. Xing, N. Mathews, S. S. Lim, N. Yantara, X. Liu, D. Sabba, M. Grätzel, S. Mhaisalkar, T. C. Sum, *Nat Mater* **2014**, *13*, 476.

[8] K. Hwang, Y.-S. Jung, Y.-J. Heo, F. H. Scholes, S. E. Watkins, J. Subbiah, D. J. Jones, D.-Y. Kim, D. Vak, *Advanced Materials* **2015**, *27*, 1241.

[9] Z. Li, T. R. Klein, D. H. Kim, M. Yang, J. J. Berry, M. F. A. M. van Hest, K. Zhu, *Nature Reviews Materials* **2018**, *3*, 18017.

[10] T.-B. Song, Q. Chen, H. Zhou, C. Jiang, H.-H. Wang, Y. (Michael) Yang, Y. Liu, J. You, Y. Yang, *J. Mater. Chem. A* **2015**, *3*, 9032.

[11] Y. Chen, M. He, J. Peng, Y. Sun, Z. Liang, *Advanced Science* **2016**, *3*, 1500392.

[12] M. Jung, S.-G. Ji, G. Kim, S. I. Seok, *Chem. Soc. Rev.* **2019**, *48*, 2011.

[13] J. S. Manser, M. I. Saidaminov, J. A. Christians, O. M. Bakr, P. V. Kamat, *Acc. Chem. Res.* **2016**, *49*, 330.

[14] S. Tang, Y. Deng, X. Zheng, Y. Bai, Y. Fang, Q. Dong, H. Wei, J. Huang, *Advanced Energy Materials* **2017**, *7*, 1700302.

[15] N. J. Jeon, J. H. Noh, Y. C. Kim, W. S. Yang, S. Ryu, S. I. Seok, *Nat Mater* **2014**, *13*, 897.

[16] B. J. Kim, S. Lee, H. S. Jung, *J. Mater. Chem. A* **2018**, *6*, 12215.

[17] A. Ng, Z. Ren, H. Hu, P. W. K. Fong, Q. Shen, S. H. Cheung, P. Qin, J.-W. Lee, A. B. Djurišić, S. K. So, G. Li, Y. Yang, C. Surya, *Advanced Materials* **2018**, *30*, 1804402.

[18] X. Cao, L. Zhi, Y. Jia, Y. Li, K. Zhao, X. Cui, L. Ci, D. Zhuang, J. Wei, *ACS Appl. Mater. Interfaces* **2019**, *11*, 7639.

[19] J.-H. Im, H.-S. Kim, N.-G. Park, *APL Materials* **2014**, *2*, 081510.

[20] C.-C. Chen, Z. Hong, G. Li, Q. Chen, H. Zhou, Y. Yang, *JPE* **2015**, *5*, 057405.

[21] M. Saliba, J.-P. Correa-Baena, C. M. Wolff, M. Stolterfoht, N. Phung, S. Albrecht, D. Neher, A. Abate, *Chem. Mater.* **2018**, *30*, 4193.

[22] T.-B. Song, I. D. Sharp, C. M. Sutter-Fella, *J. Phys. Energy* **2018**, *1*, 011002.

[23] Q. Hu, L. Zhao, J. Wu, K. Gao, D. Luo, Y. Jiang, Z. Zhang, C. Zhu, E. Schaible, A. Hexemer, C. Wang, Y. Liu, W. Zhang, M. Grätzel, F. Liu, T. P. Russell, R. Zhu, Q. Gong, *Nature Communications* **2017**, *8*, 15688.

[24] T. Miyadera, Y. Shibata, T. Koganezawa, T. N. Murakami, T. Sugita, N. Tanigaki, M. Chikamatsu, *Nano Lett.* **2015**, *15*, 5630.

[25] D. T. Moore, H. Sai, K. W. Tan, D.-M. Smilgies, W. Zhang, H. J. Snaith, U. Wiesner, L. A. Estroff, *J. Am. Chem. Soc.* **2015**, *137*, 2350.

[26] W. Zhang, M. Saliba, D. T. Moore, S. K. Pathak, M. T. Hörantner, T. Stergiopoulos, S. D. Stranks, G. E. Eperon, J. A. Alexander-Webber, A. Abate, A. Sadhanala, S. Yao, Y. Chen, R. H. Friend, L. A. Estroff, U. Wiesner, H. J. Snaith, *Nature Communications* **2015**, *6*, 6142.

[27] E. L. Unger, A. R. Bowring, C. J. Tassone, V. L. Pool, A. Gold-Parker, R. Cheacharoen, K. H. Stone, E. T. Hoke, M. F. Toney, M. D. McGehee, *Chem. Mater.* **2014**, *26*, 7158.
[28] Y. Zhong, R. Munir, J. Li, M.-C. Tang, M. R. Niazi, D.-M. Smilgies, K. Zhao, A. Amassian, *ACS Energy Lett.* **2018**, 1078.
[29] R. Munir, A. D. Sheikh, M. Abdelsamie, H. Hu, L. Yu, K. Zhao, T. Kim, O. E. Tall, R. Li, D.-M. Smilgies, A. Amassian, *Advanced Materials* **2017**, *29*, 1604113.
[30] D. P. Nenon, J. A. Christians, L. M. Wheeler, J. L. Blackburn, E. M. Sanehira, B. Dou, M. L. Olsen, K. Zhu, J. J. Berry, J. M. Luther, *Energy Environ. Sci.* **2016**, *9*, 2072.
[31] P. Pistor, J. Borchert, W. Fränzel, R. Csuk, R. Scheer, *J. Phys. Chem. Lett.* **2014**, *5*, 3308.
[32] S. J. Park, A. R. Kim, J. T. Hong, J. Y. Park, S. Lee, Y. H. Ahn, *J. Phys. Chem. Lett.* **2017**, *8*, 401.
[33] M. Alsari, O. Bikondoa, J. Bishop, M. Abdi-Jalebi, L. Y. Ozer, M. Hampton, P. Thompson, M. T. Hörantner, S. Mahesh, C. Greenland, J. E. Macdonald, G. Palmisano, H. J. Snaith, D. G. Lidzey, S. D. Stranks, R. H. Friend, S. Lilliu, *Energy Environ. Sci.* **2018**, *11*, 383.
[34] J. A. Aguiar, S. Wozny, T. G. Holesinger, T. Aoki, M. K. Patel, M. Yang, J. J. Berry, M. Al-Jassim, W. Zhou, K. Zhu, *Energy Environ. Sci.* **2016**, *9*, 2372.
[35] J. J. van Franeker, K. H. Hendriks, B. J. Bruijnaers, M. W. G. M. Verhoeven, M. M. Wienk, R. A. J. Janssen, *Advanced Energy Materials* **2017**, *7*, 1601822.
[36] L. Zhao, D. Luo, J. Wu, Q. Hu, W. Zhang, K. Chen, T. Liu, Y. Liu, Y. Zhang, F. Liu, T. P. Russell, H. J. Snaith, R. Zhu, Q. Gong, *Advanced Functional Materials* **2016**, *26*, 3508.
[37] R. Brenes, C. Eames, V. Bulović, M. S. Islam, S. D. Stranks, *Advanced Materials* **2018**, *30*, 1706208.
[38] P. Fassl, V. Lami, A. Bausch, Z. Wang, M. T. Klug, H. J. Snaith, Y. Vaynzof, *arXiv:1904.11767 [physics]* **2019**.
[39] L. Li, P. Zhou, J. Li, Y. Mo, W. Huang, J. Xiao, W. Li, Z. Ku, J. Zhong, Y. Peng, Y.-B. Cheng, F. Huang, *J. Mater. Chem. C* **2018**, *6*, 13157.
[40] R. Brenes, D. Guo, A. Osherov, N. K. Noel, C. Eames, E. M. Hutter, S. K. Pathak, F. Niroui, R. H. Friend, M. S. Islam, H. J. Snaith, V. Bulović, T. J. Savenije, S. D. Stranks, *Joule* **2017**, *1*, 155.
[41] A. A. Petrov, I. P. Sokolova, N. A. Belich, G. S. Peters, P. V. Dorovatovskii, Y. V. Zubavichus, V. N. Khrustalev, A. V. Petrov, M. Grätzel, E. A. Goodilin, A. B. Tarasov, *J. Phys. Chem. C* **2017**, *121*, 20739.
[42] R. W. Schaeffer, M. Ardelean, *Powder Diffraction* **2001**, *16*, 16.
[43] H. Yu, F. Wang, F. Xie, W. Li, J. Chen, N. Zhao, *Advanced Functional Materials* **2014**, *24*, 7102.
[44] S. T. Williams, F. Zuo, C.-C. Chueh, C.-Y. Liao, P.-W. Liang, A. K.-Y. Jen, *ACS Nano* **2014**, *8*, 10640.
[45] Q. Dong, Y. Yuan, Y. Shao, Y. Fang, Q. Wang, J. Huang, *Energy Environ. Sci.* **2015**, *8*, 2464.
[46] S. Paek, P. Schouwink, E. N. Athanasopoulou, K. T. Cho, G. Grancini, Y. Lee, Y. Zhang, F. Stellacci, M. K. Nazeeruddin, P. Gao, *Chem. Mater.* **2017**, *29*, 3490.
[47] M. Xiao, F. Huang, W. Huang, Y. Dkhissi, Y. Zhu, J. Etheridge, A. Gray-Weale, U. Bach, Y.-B. Cheng, L. Spiccia, *Angewandte Chemie* **2014**, *126*, 10056.
[48] S. D. Stranks, V. M. Burlakov, T. Leijtens, J. M. Ball, A. Goriely, H. J. Snaith, *Phys. Rev. Applied* **2014**, *2*, 034007.

[49] S. D. Stranks, *ACS Energy Lett.* **2017**, *2*, 1515.
[50] F. Deschler, M. Price, S. Pathak, L. E. Klintberg, D.-D. Jarausch, R. Higler, S. Hüttner, T. Leijtens, S. D. Stranks, H. J. Snaith, M. Atatüre, R. T. Phillips, R. H. Friend, *J. Phys. Chem. Lett.* **2014**, *5*, 1421.
[51] R. L. Milot, G. E. Eperon, H. J. Snaith, M. B. Johnston, L. M. Herz, *Adv. Funct. Mater.* **2015**, *25*, 6218.
[52] L. Wagner, L. E. Mundt, G. Mathiazhagan, M. Mundus, M. C. Schubert, S. Mastroianni, U. Würfel, A. Hinsch, S. W. Glunz, *Sci Rep* **2017**, *7*, 1.
[53] T.-Y. Hsieh, C.-K. Huang, T.-S. Su, C.-Y. Hong, T.-C. Wei, *ACS Appl. Mater. Interfaces* **2017**, *9*, 8623.
[54] T. Unold, L. Gütay, in *Advanced Characterization Techniques for Thin Film Solar Cells* (Eds.: D. Abou-Ras, T. Kirchartz, U. Rau), Wiley-VCH Verlag GmbH & Co. KGaA, Weinheim, Germany, **2011**, pp. 151–175.
[55] T. H. Gfroerer, in *Encyclopedia of Analytical Chemistry*, John Wiley & Sons, Ltd, Chichester, UK, **2006**, pp. 9209–9231.
[56] W. Nie, H. Tsai, R. Asadpour, J.-C. Blancon, A. J. Neukirch, G. Gupta, J. J. Crochet, M. Chhowalla, S. Tretiak, M. A. Alam, H.-L. Wang, A. D. Mohite, *Science* **2015**, *347*, 522.
[57] Q. A. Akkerman, S. G. Motti, A. R. Srimath Kandada, E. Mosconi, V. D'Innocenzo, G. Bertoni, S. Marras, B. A. Kamino, L. Miranda, F. De Angelis, A. Petrozza, M. Prato, L. Manna, *J. Am. Chem. Soc.* **2016**, *138*, 1010.
[58] M. Do, I. Kim, M. A. Kolaczkowski, J. Kang, G. A. Kamat, Z. Yuan, N. S. Barchi, L.-W. Wang, Y. Liu, M. J. Jurow, C. M. Sutter-Fella, *Nanoscale* **2019**, DOI 10.1039/C9NR04010B.
[59] Y. Tian, M. Peter, E. Unger, M. Abdellah, K. Zheng, T. Pullerits, A. Yartsev, V. Sundström, I. G. Scheblykin, *Phys. Chem. Chem. Phys.* **2015**, *17*, 24978.
[60] J. F. Galisteo-López, M. Anaya, M. E. Calvo, H. Míguez, *J. Phys. Chem. Lett.* **2015**, *6*, 2200.
[61] A. Ummadisingu, L. Steier, J.-Y. Seo, T. Matsui, A. Abate, W. Tress, M. Grätzel, *Nature* **2017**, *545*, 208.
[62] F. Zheng, W. Chen, T. Bu, K. P. Ghiggino, F. Huang, Y. Cheng, P. Tapping, T. W. Kee, B. Jia, X. Wen, *Advanced Energy Materials* **2019**, *0*, 1901016.
[63] F. K. Aldibaja, L. Badia, E. Mas-Marzá, R. S. Sánchez, E. M. Barea, I. Mora-Sero, *J. Mater. Chem. A* **2015**, *3*, 9194.
[64] Q. Chen, H. Zhou, T.-B. Song, S. Luo, Z. Hong, H.-S. Duan, L. Dou, Y. Liu, Y. Yang, *Nano Lett.* **2014**, *14*, 4158.
[65] Q. Jiang, Z. Chu, P. Wang, X. Yang, H. Liu, Y. Wang, Z. Yin, J. Wu, X. Zhang, J. You, *Advanced Materials* **2017**, *29*, 1703852.
[66] M. Saliba, *Advanced Energy Materials* **2019**, *9*, 1803754.
[67] N. Tamura, in *Strain and Dislocation Gradients from Diffraction*, IMPERIAL COLLEGE PRESS, **2013**, pp. 125–155.

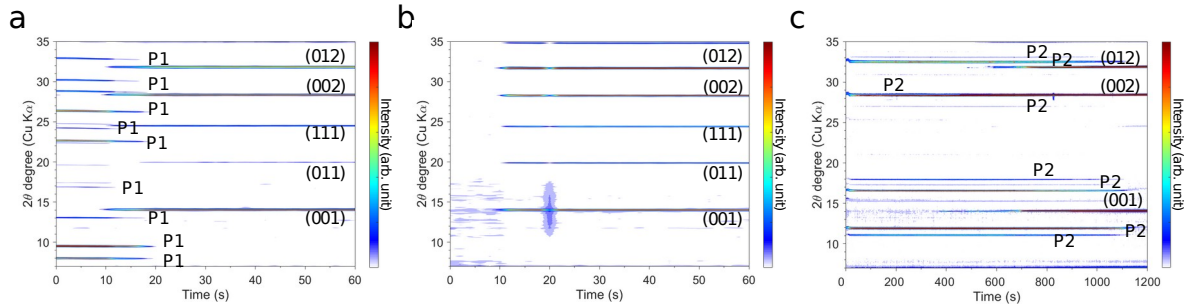

Figure 1. ***In situ*** **synchrotron diffraction. a**, **b**, and **c** diffraction measurements (χ = 35° integration of the 2D diffraction patterns) during annealing of different perovskite precursor solutions employing PbI_2, $PbAc_2$, and $PbCl_2$ routes, respectively, at 110 ºC on glass substrates. Perovskite diffraction peaks are labeled according to a pseudo-cubic crystal symmetry. Precursor phases are labeled with P1 and P2 and are discussed in the main text.

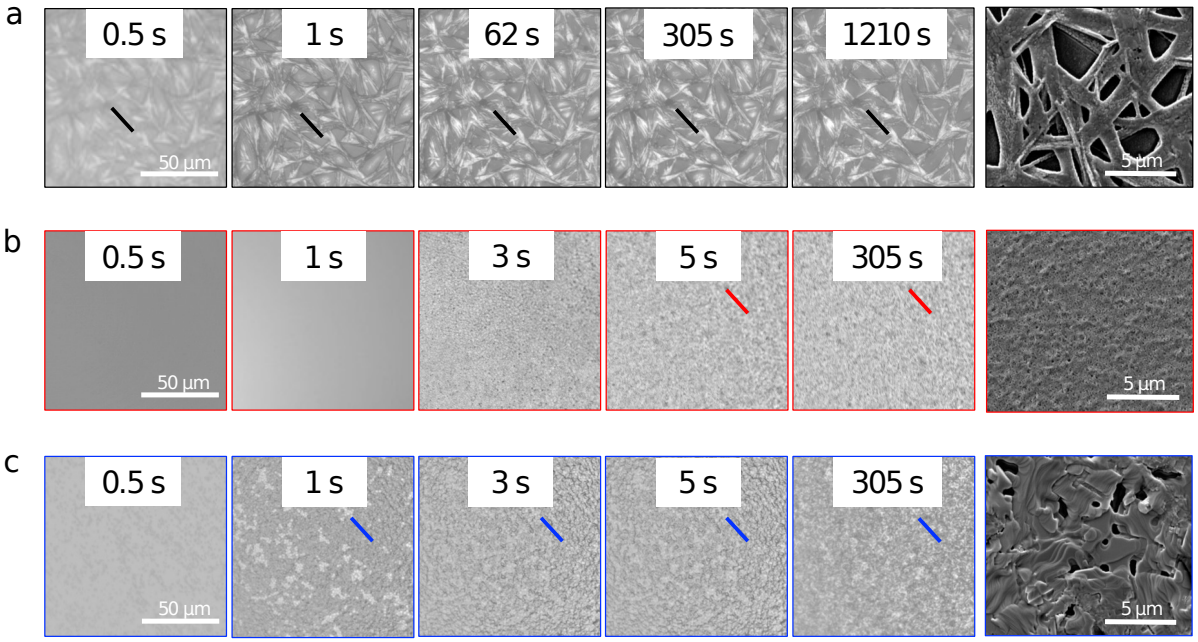

Figure 2. ***In situ*** **optical microscopy. a**, **b**, and **c** optical microscope images measured during annealing of different perovskite precursor solutions employing PbI_2, $PbAc_2$, or $PbCl_2$ routes,

respectively, at 110 ºC on glass substrates. The time stamp is given at the top of each image and the arrow can be used as a tracker for the same sample spot. The right-hand side illustrates corresponding SEM images after 30 min annealing.

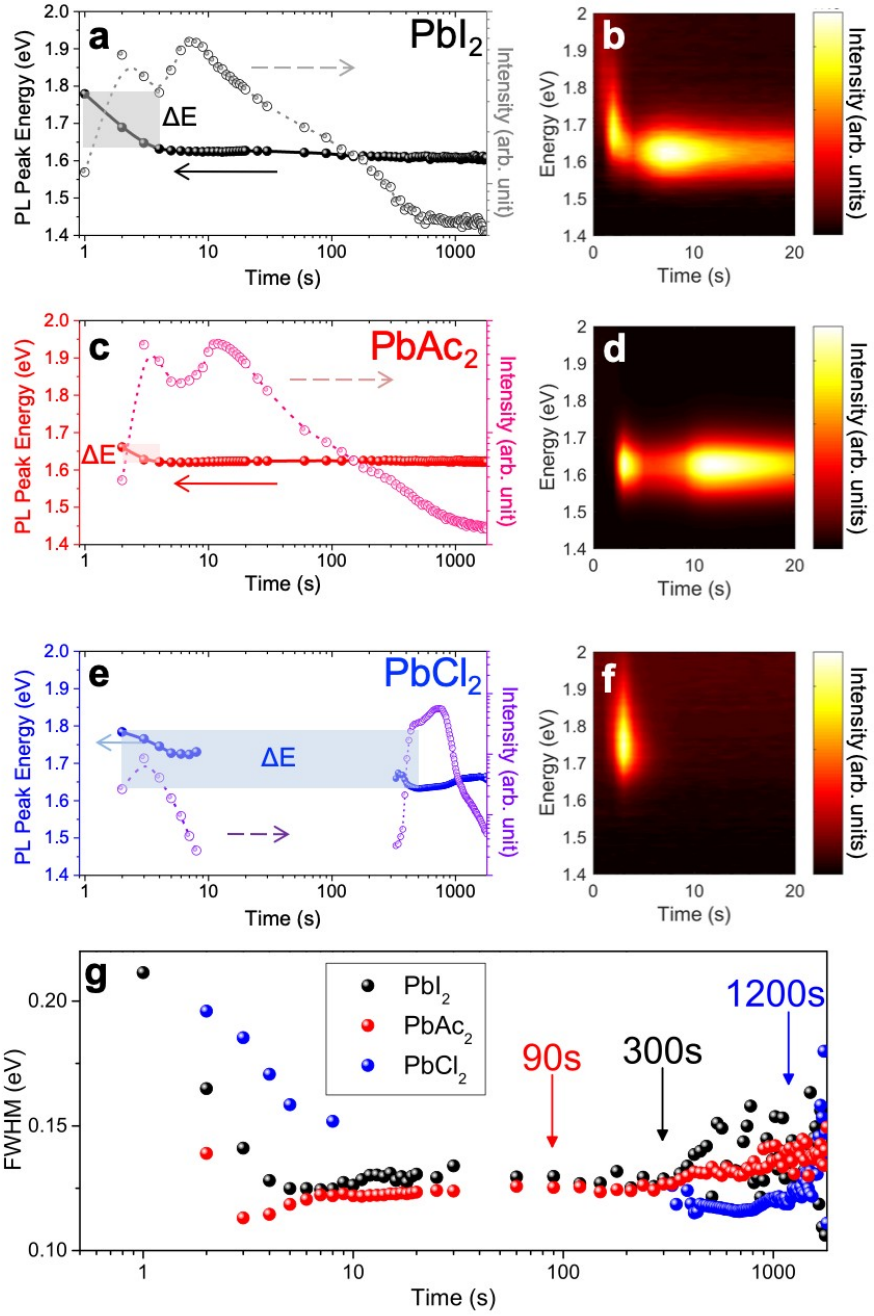

Figure 3. ***In situ*** **photoluminescence. a**, **c**, and **e** PL signal measured during annealing of different perovskite precursor solutions employing PbI_2, $PbAc_2$, or $PbCl_2$ routes, respectively, during annealing at 110 ºC on glass substrates. PL peak position and intensity are illustrated. The shaded areas illustrate ΔE which is defined as the difference of initial and final PL emission energy. **b**, **d** and **f**, contour maps of the emission energy within the first 20 s of annealing. **g** Full width at half maxima (FWHM) extracted by Gaussian peak fitting of the

emission spectra. The specified times indicate decomposition-related appearance of PbI_2 phase.

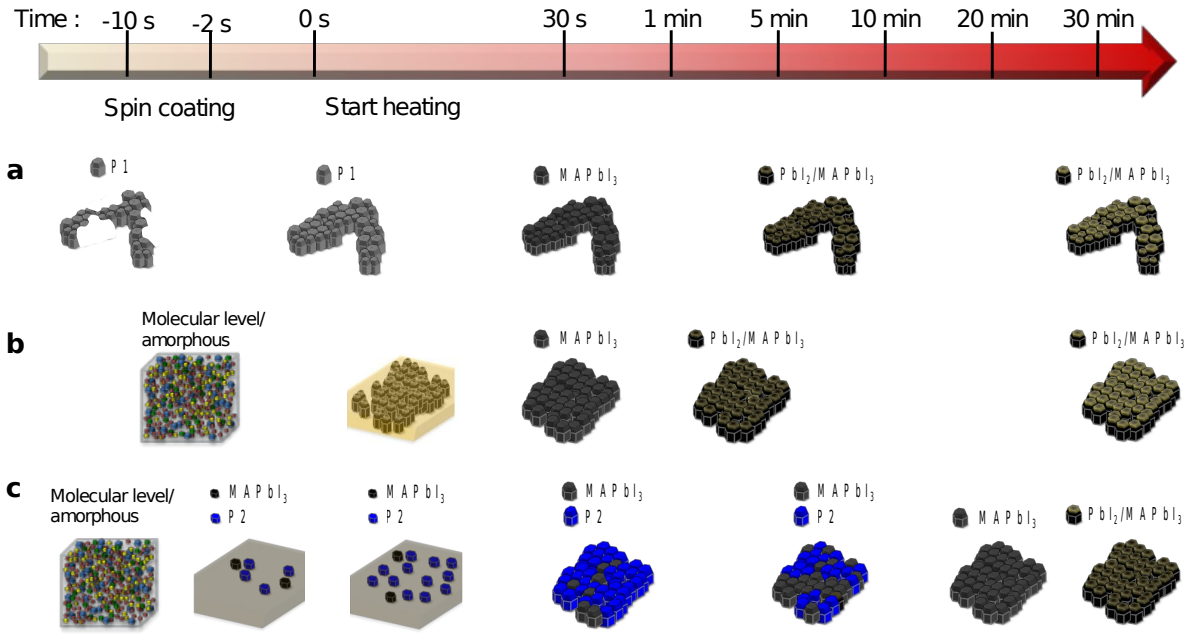

Figure 4. Schematic illustration of $MAPbI_3$ film formation. a, **b**, and **c** perovskite film formation stages depicted over time for the PbI_2, $PbAc_2$, and $PbCl_2$ routes, respectively. Morphology is defined within the first seconds of annealing. P1 and P2 are precursor phases. P1 is assigned to $(MA)_2(DMF)_2Pb_3I_8$.

Revealing the dynamics of hybrid metal halide perovskite formation via multi-modal *in situ* probes

*Tze-Bin Song, Zhenghao Yuan, Megumi Mori, Faizan Motiwala, Gideon Segev, Eloïse Masquelier, Camelia V. Stan, Jonathan L. Slack, Nobumichi Tamura, Carolin M. Sutter-Fella**

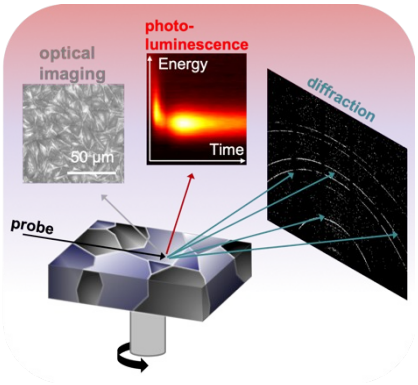

The same unique properties that make lead halide perovskites remarkable solar energy conversion materials will also drive applications in other optoelectronic devices as we learn more about their formation. Insights are provided here by truly monitoring the *in situ* evolution of crystal phase, morphology, and optoelectronic properties correlated to precursor chemistry.

Supporting Information

Revealing the dynamics of hybrid metal halide perovskite formation via multi-modal *in situ* probes

*Tze-Bin Song, Zhenghao Yuan, Megumi Mori, Faizan Motiwala, Gideon Segev, Eloïse Masquelier, Camelia V. Stan, Jonathan L. Slack, Nobumichi Tamura, Carolin M. Sutter-Fella**

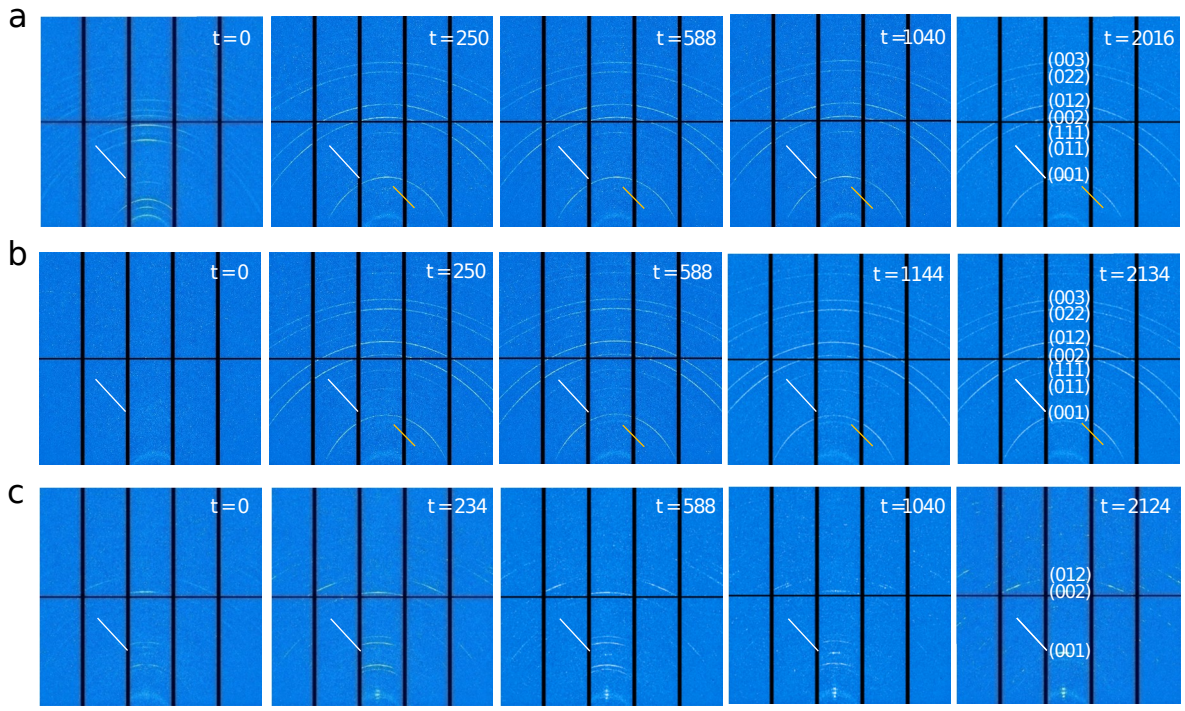

Figure S1. 2D diffraction patterns. Time evolution of the *in situ* diffraction signal following the **a**, PbI_2; **b**, $PbAc_2$; **c**, $PbCl_2$-routes to form $MAPbI_3$ films. White arrow: diffraction from $MAPbI_3$; Yellow arrow: diffraction from PbI_2. Experimental conditions: synthesis and annealing in synchrotron hutch (ALS beamline 12.3.2), drying at 110ºC, glass substrate.

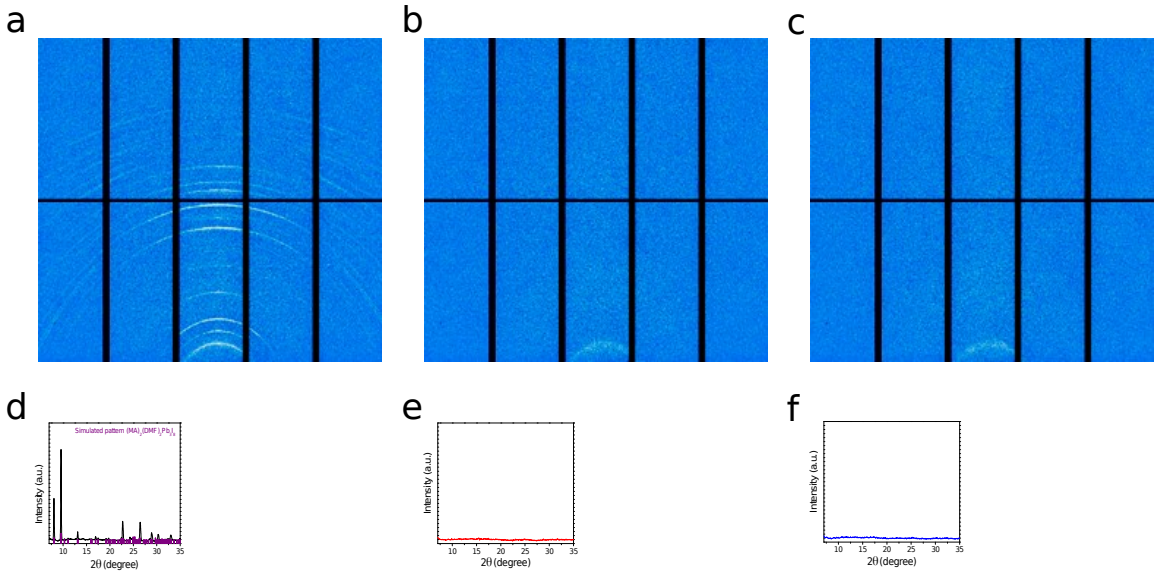

Figure S2. Diffraction patterns during spin-coating process (10s before annealing): 2D patterns (a-c) and integrated patterns (d-f) following the **a+d**, PbI_2; **b+e**, $PbAc_2$; **c+f**, $PbCl_2$-routes to form $MAPbI_3$ films. Experimental conditions: synthesis in synchrotron hutch (ALS beamline 12.3.2), taken during spin-coating (i.e. no drying), glass substrate. Simulated pattern for $(MA)_2(DMF)_2Pb_3I_8$ structure from reference [1].

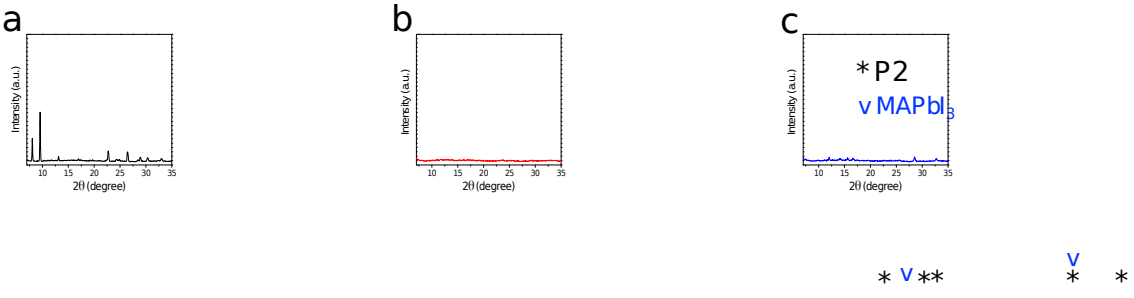

Figure S3. Diffraction patterns during spin-coating process (2s before annealing) following the a, PbI_2; b, $PbAc_2$; and **c, $PbCl_2$-routes to form $MAPbI_3$ films.** Experimental conditions: synthesis in synchrotron hutch (ALS beamline 12.3.2), taken during spin-coating (i.e. no drying), glass substrate.

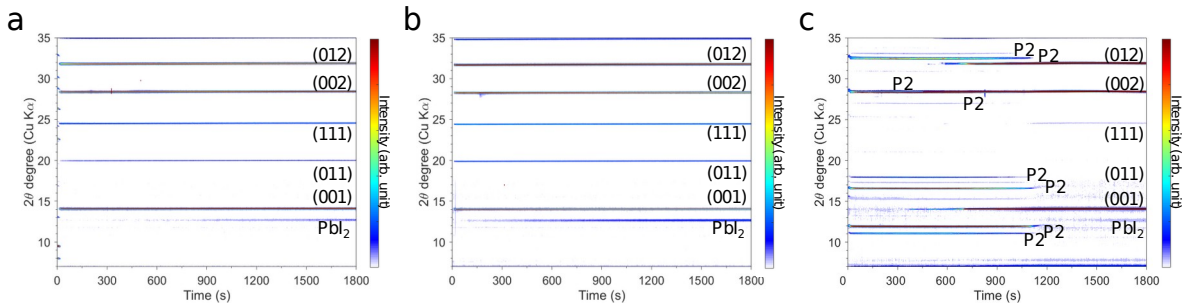

Figure S4. Diffraction patterns (χ = 35° integration of the 2D diffraction patterns). Time evolution of the *in situ* diffraction signal following the **a**, PbI_2; **b**, $PbAc_2$; **c**, $PbCl_2$-routes to form $MAPbI_3$ films. Experimental conditions: synthesis and annealing in synchrotron hutch (ALS beamline 12.3.2), drying at 110ºC, glass substrate.

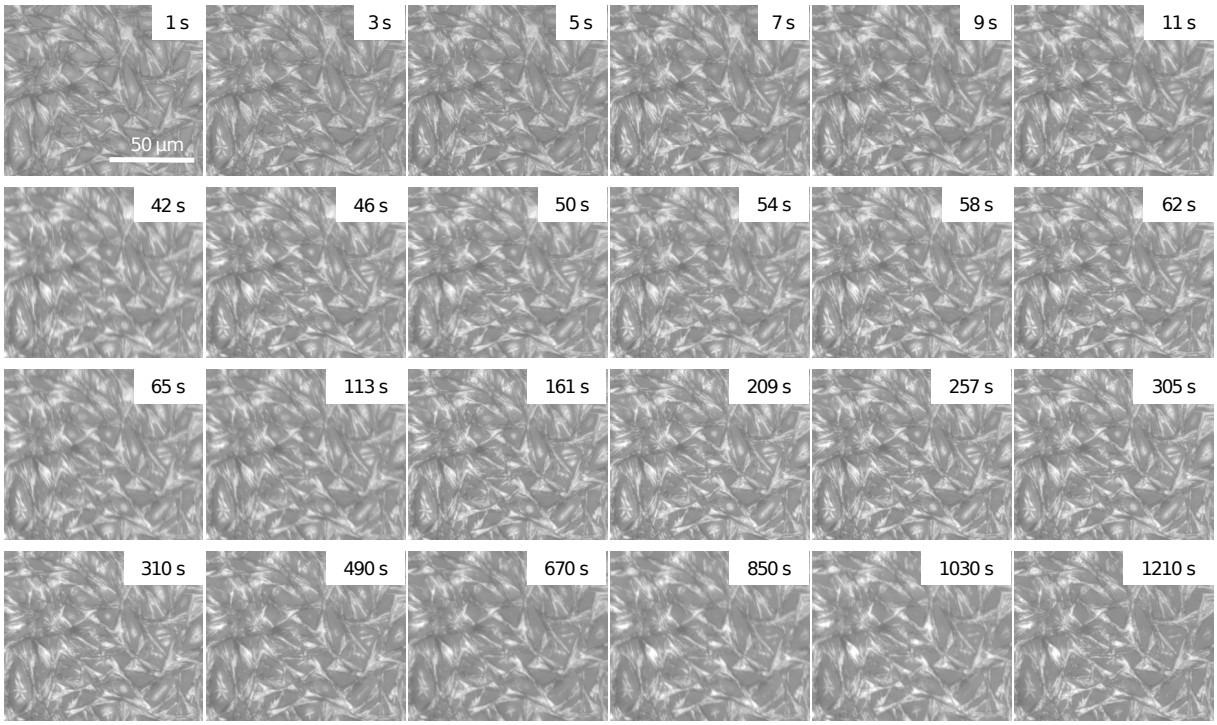

Figure S5. Optical microscope imaging series: Time evolution of the *in situ* microscope images following the PbI_2-route to form $MAPbI_3$ films. Experimental conditions: synthesis and annealing in fume hood, drying at 110ºC, glass substrate.

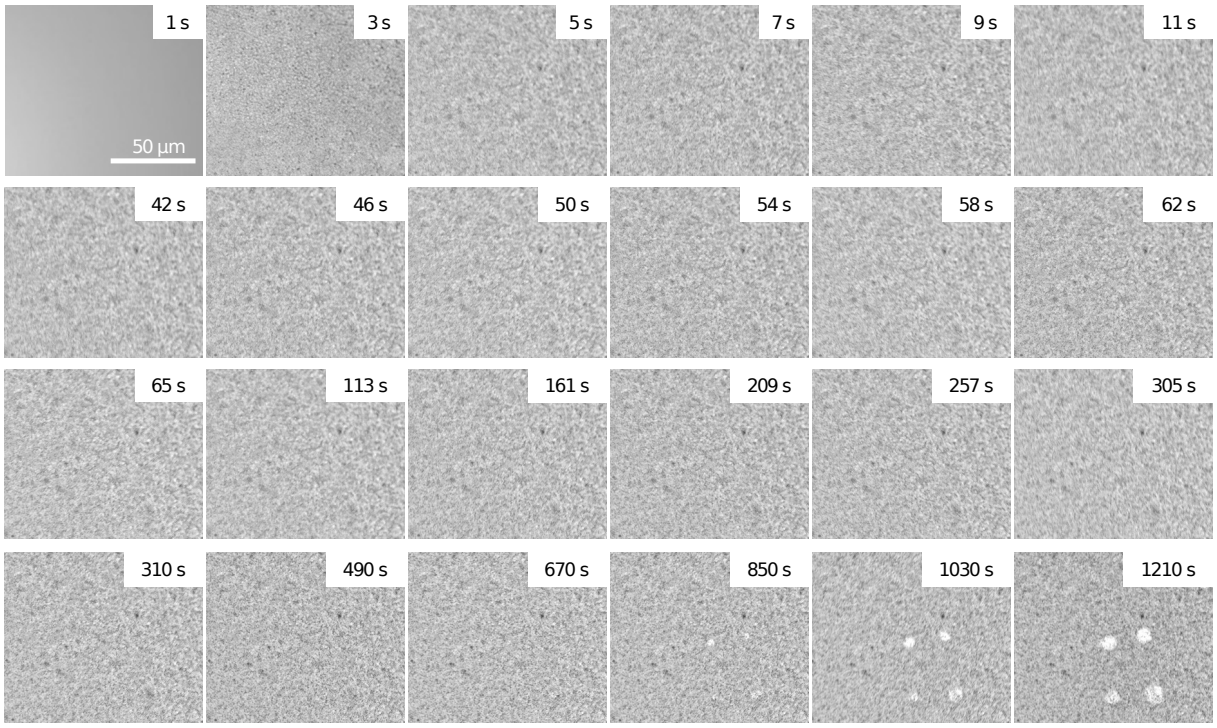

Figure S6. Optical microscope imaging series: Time evolution of the *in situ* microscope images following the $PbAc_2$-route to form $MAPbI_3$ films. Bright spots appearing towards the end of the annealing are related to PbI_2 formation. Experimental conditions: synthesis and annealing in fume hood, drying at 110ºC, glass substrate.

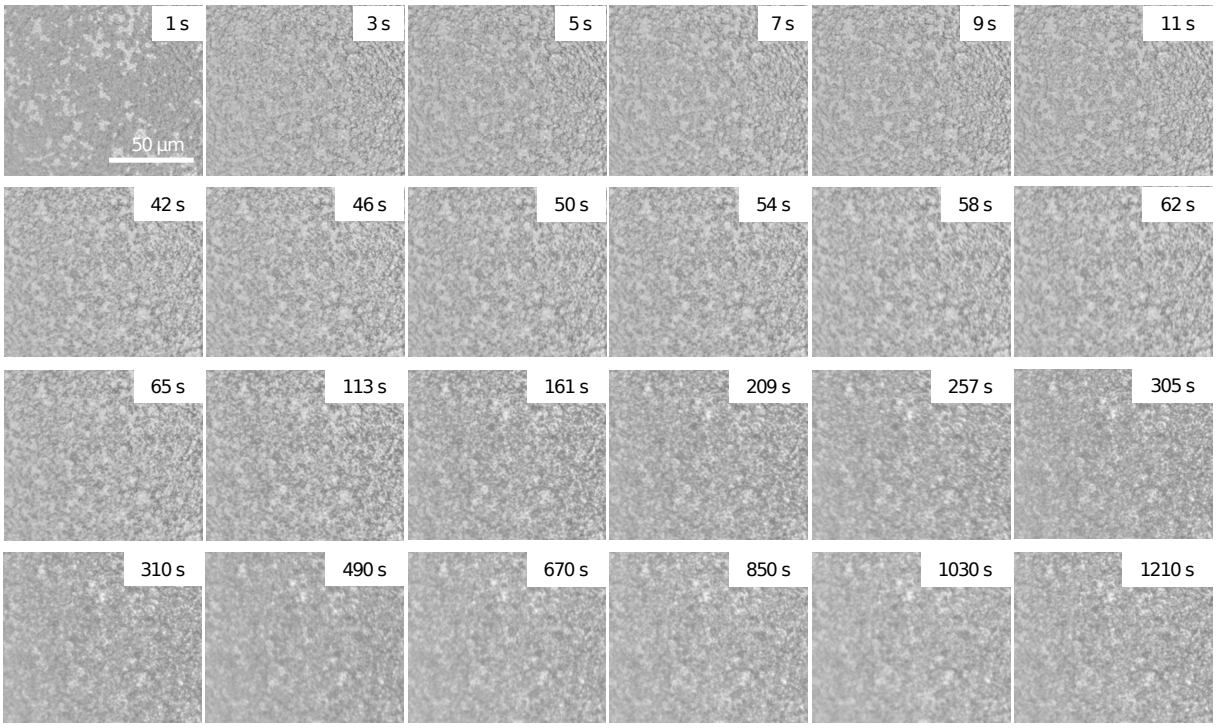

Figure S7. Optical microscope imaging series: Time evolution of the *in situ* microscope images following the $PbCl_2$-route to form $MAPbI_3$ films. Experimental conditions: synthesis and annealing in fume hood, drying at 110ºC, glass substrate.

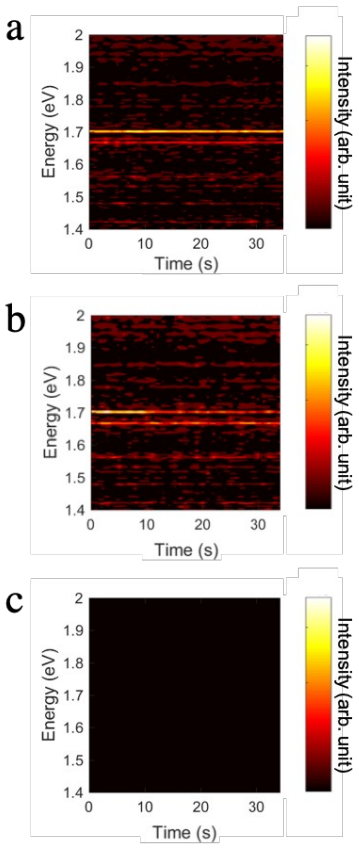

Figure S8. PL during spin-coating. Time evolution of the *in situ* PL signal following the PbI_2, $PbAc_2$, and $PbCl_2$-routes (a-c) to form $MAPbI_3$ films. Measurements are taken on the spin-coater (500 rpm for 5 s followed by 2,000 rpm for 30 s) in the fume hood, no annealing. The bright lines around 1.7 eV in a and b are from the spectrometer background and are not related to the sample response.

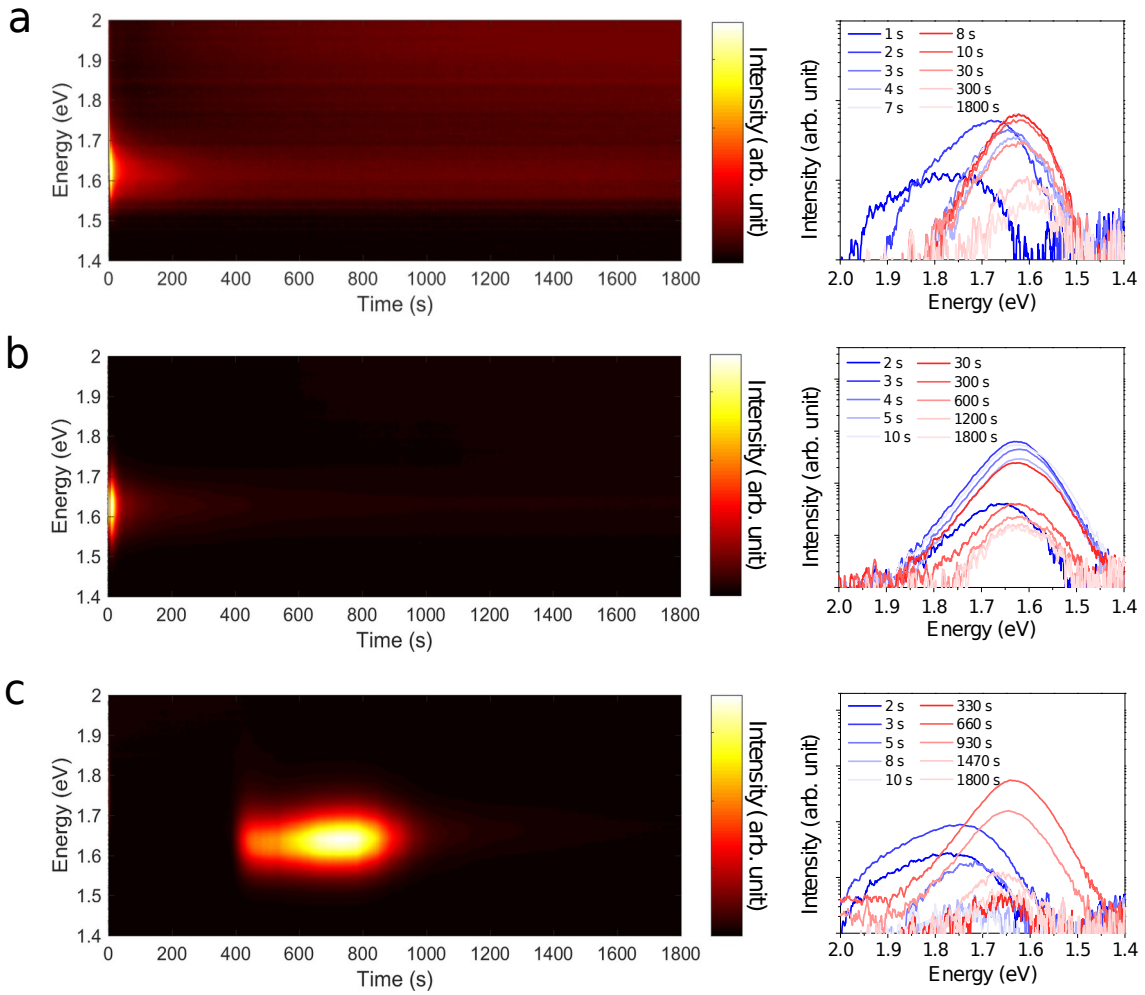

Figure S9. Time evolution of the *in situ* PL signal following the a, PbI_2; b, $PbAc_2$; and c, $PbCl_2$-routes to form $MAPbI_3$ films. The right-hand side represents the corresponding individual PL spectra at selected times. Experimental conditions: synthesis and annealing in fume hood at 110ºC, glass substrate.

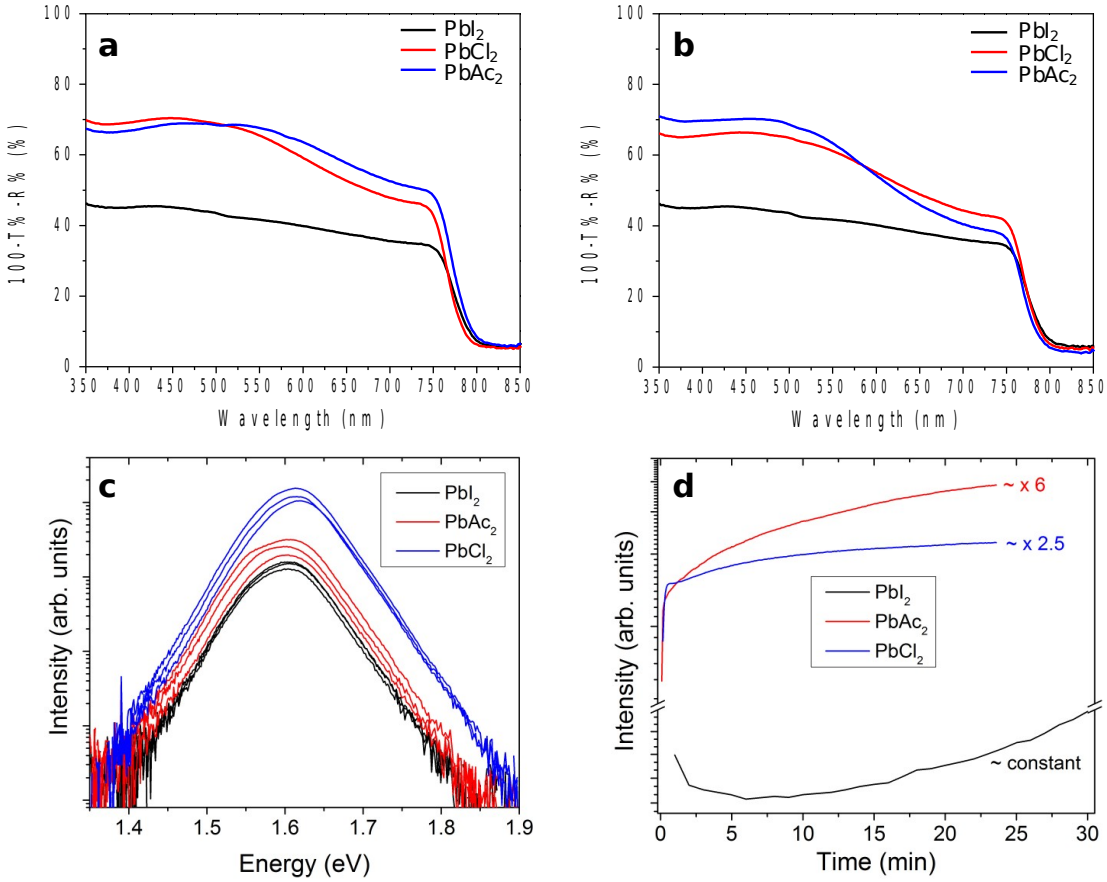

Figure S10. Ex situ optical characterization. UV Vis of $MAPbI_3$ films annealed for **a** 15 min and **b** 30 min. Spot-to-spot steady state PL measurements **c** and PL peak intensity over time at room temperature **d**. Excitation density for the PL measurements ~30 mW/cm^2 (532 nm continuous wave laser diode). Experimental conditions: synthesis and annealing in fume hood, drying at 110ºC, glass substrate.

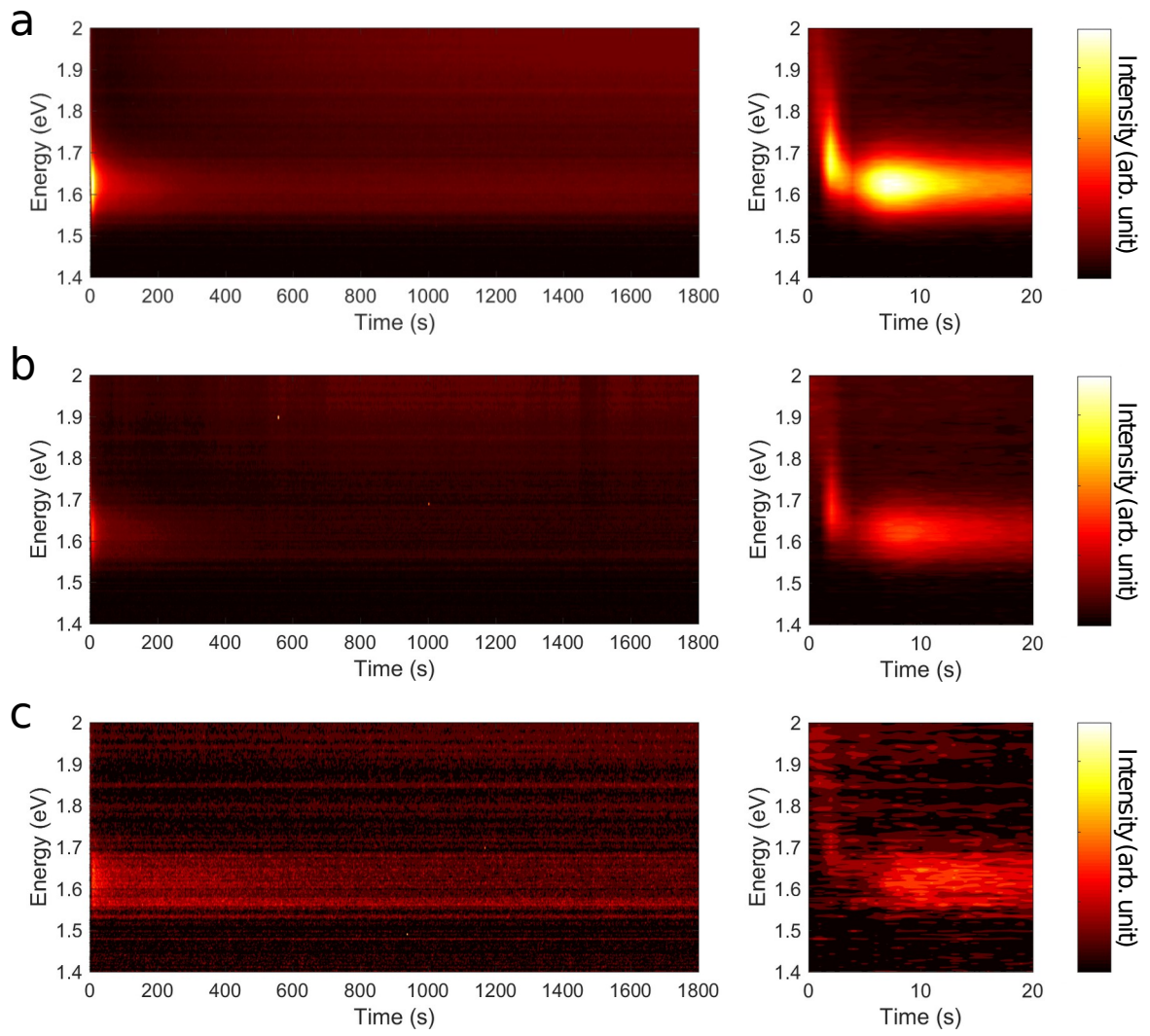

Figure S11. Effect of laser excitation density on PL: Time evolution of the *in situ* PL signal following the PbI_2-route to form $MAPbI_3$ films. **a**, 30 mW/cm^2; **b**, 15 mW/cm^2; **c**, 6 mW/cm^2. Experimental conditions: synthesis and annealing in fume hood, drying at 110ºC, glass substrate.

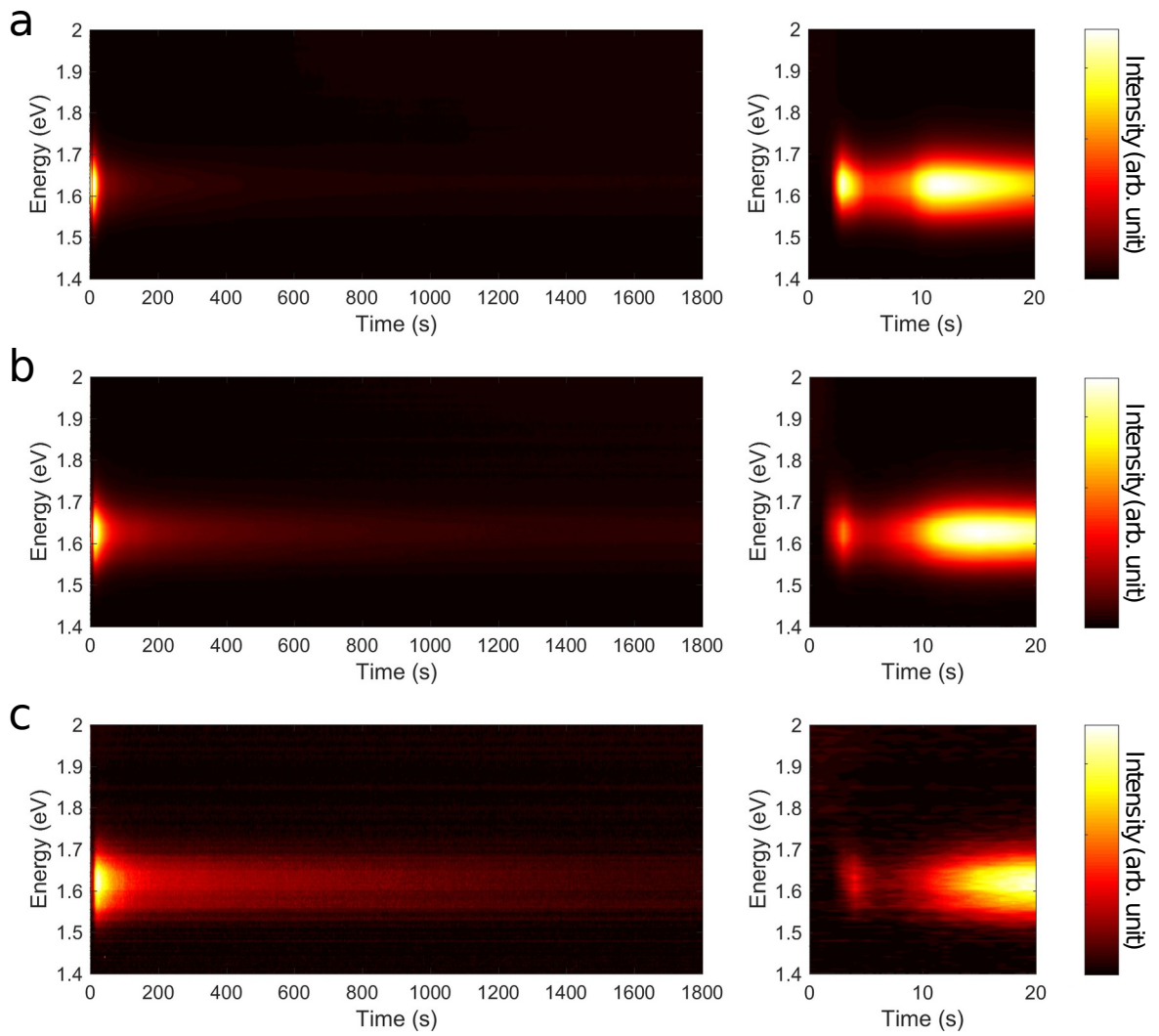

Figure S12. Effect of laser excitation density on PL:Time evolution of the *in situ* PL signal following the $PbAc_2$-route to form $MAPbI_3$ films. a, 30 mW/cm^2; **b**, 15 mW/cm^2; **c**, 6 mW/cm^2. Experimental conditions: synthesis and annealing in fume hood, drying at 110ºC, glass substrate.

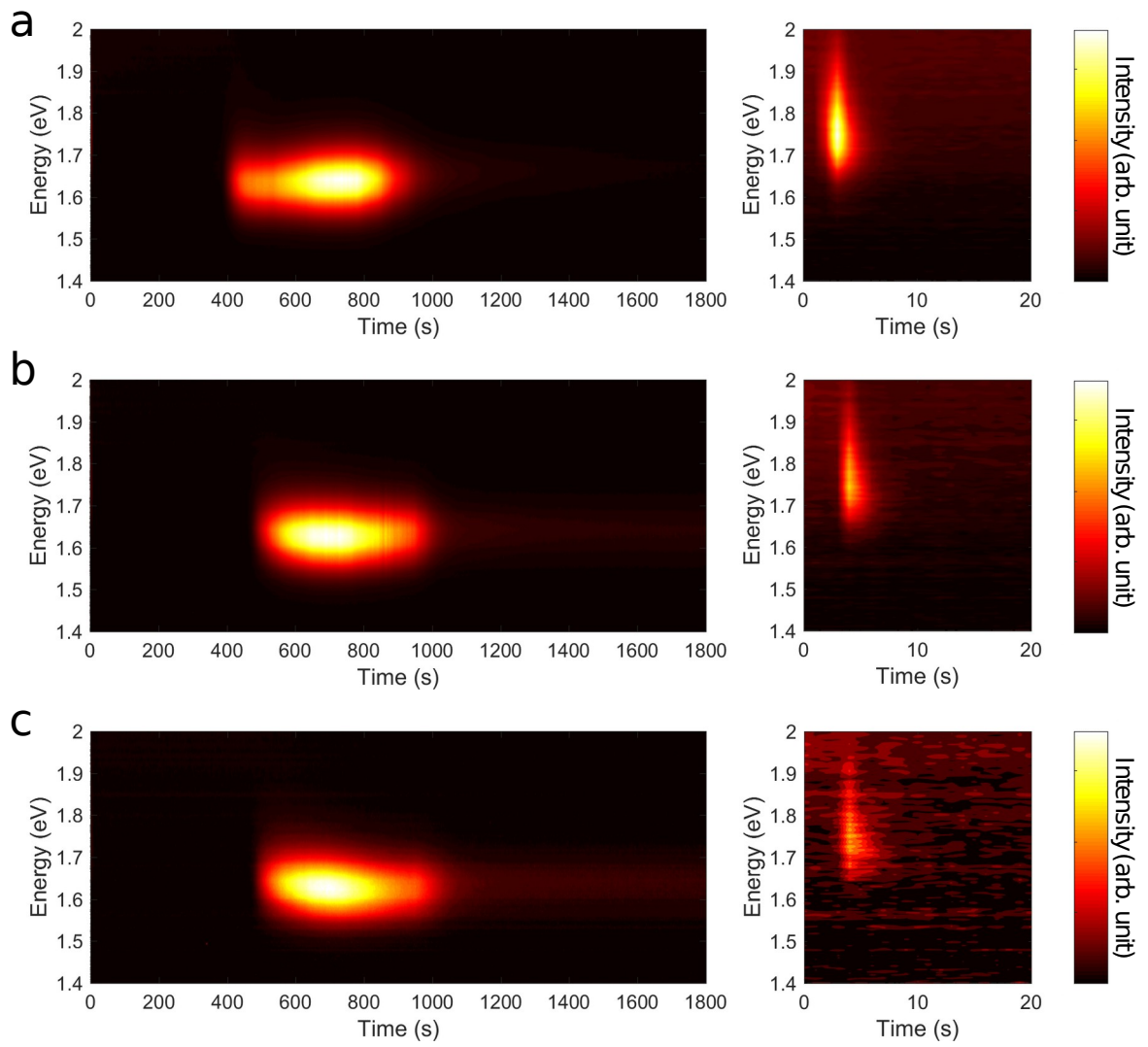

Figure S13. Effect of laser excitation density on PL: Time evolution of the *in situ* PL signal following the $PbCl_2$-route to form $MAPbI_3$ films. **a**, 30 mW/cm^2; **b**, 15 mW/cm^2; **c**, 6 mW/cm^2. Experimental conditions: synthesis and annealing in fume hood, drying at 110ºC, glass substrate.

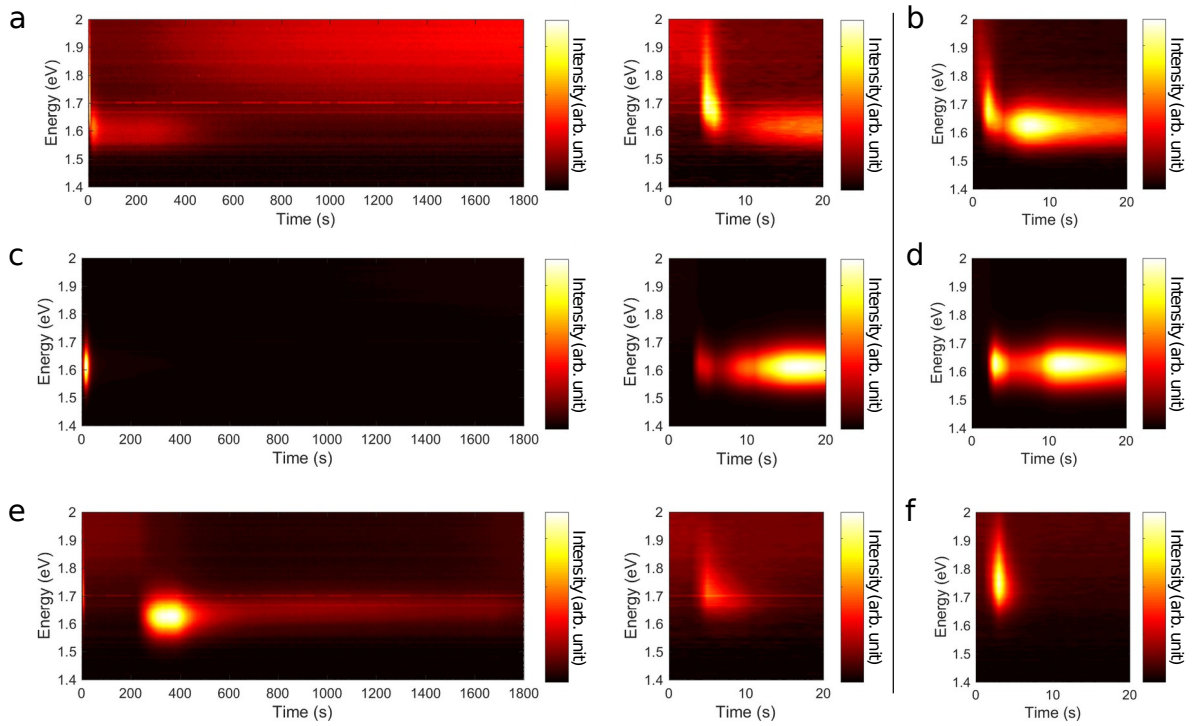

Figure S14. Effect of substrate on PL. Time evolution of the *in situ* PL signal following the **a**, PbI_2; **c**, $PbAc_2$; **e**, $PbCl_2$-routes to form $MAPbI_3$ films on FTO/SnO_2 versus glass substrate (**b**, PbI_2; **d**, $PbAc_2$; **f**, $PbCl_2$-routes). Experimental conditions: synthesis and annealing in fume hood, drying at 110ºC.

In supplemental Figure S14 we show PL during drying of the three different Pb-routes spin coated onto glass versus FTO/SnO_2 coated glass. Due to the PL quenching on FTO/SnO_2 substrate we used a 10 × higher illumination intensity (~300 mW/cm^2) and found again a ΔE shift and appearance of two PL intensity maxima with very similar kinetics. Despite competing mechanisms of evolving/increasing luminescence signal caused by the formation of semiconducting phases and PL quenching due to electron injection into SnO_2 (presumably this requires sufficient charge transport, in other words charge percolation via coalesced grains such that generated charge can reach the contact interface) the film formation kinetics seem invariant if glass or FTO/SnO_2 is used as substrate.

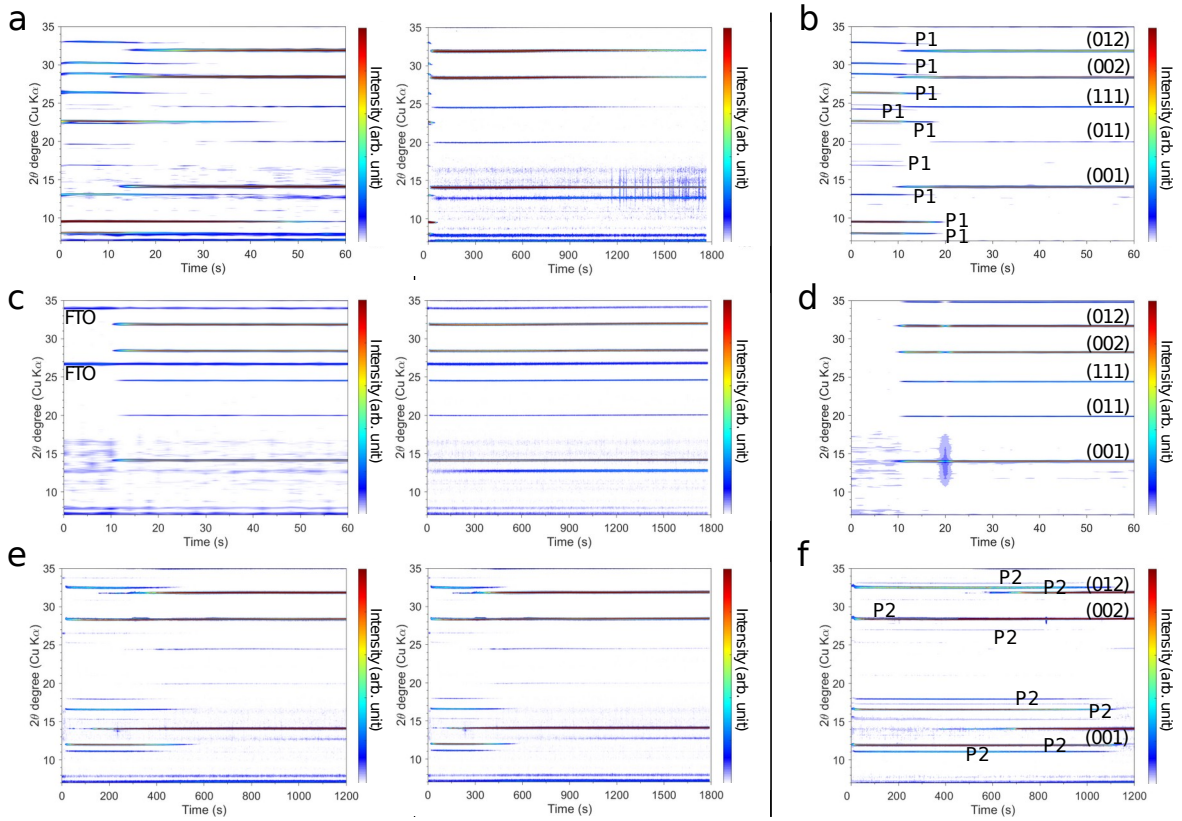

Figure S15. Effect of substrate on diffraction patterns. Time evolution of the *in situ* diffraction signal following the **a**, PbI_2; **c**, $PbAc_2$; and **e**, $PbCl_2$-routes to form $MAPbI_3$ films on FTO/SnO_2 versus glass substrates (**b**, PbI_2; **d**, $PbAc_2$; **f**, $PbCl_2$-routes). Experimental conditions: synthesis and annealing in synchrotron hutch (ALS beamline 12.3.2), drying at 110ºC.

In order to evaluate the influence of the substrate on crystallization, we also performed the *in situ* synchrotron diffraction measurements on FTO/SnO_2 coated glass substrates (Supplemental Fig. 14). All Pb-routes show the same precursor phases on FTO/SnO_2 substrates as previously described on glass substrates. Similarly, the kinetics of perovskite evolution are independent of the substrate in case of the PbI_2/$PbAc_2$ routes but are faster following the $PbCl_2$ route where precursor phases disappear after ~500 s (after ~1200 s on glass substrate) and perovskite phase is present after ~150 s (~400 s on glass substrate). Possibly, the precursor phase P2 is less stable on SnO_2 substrate than on glass substrate.

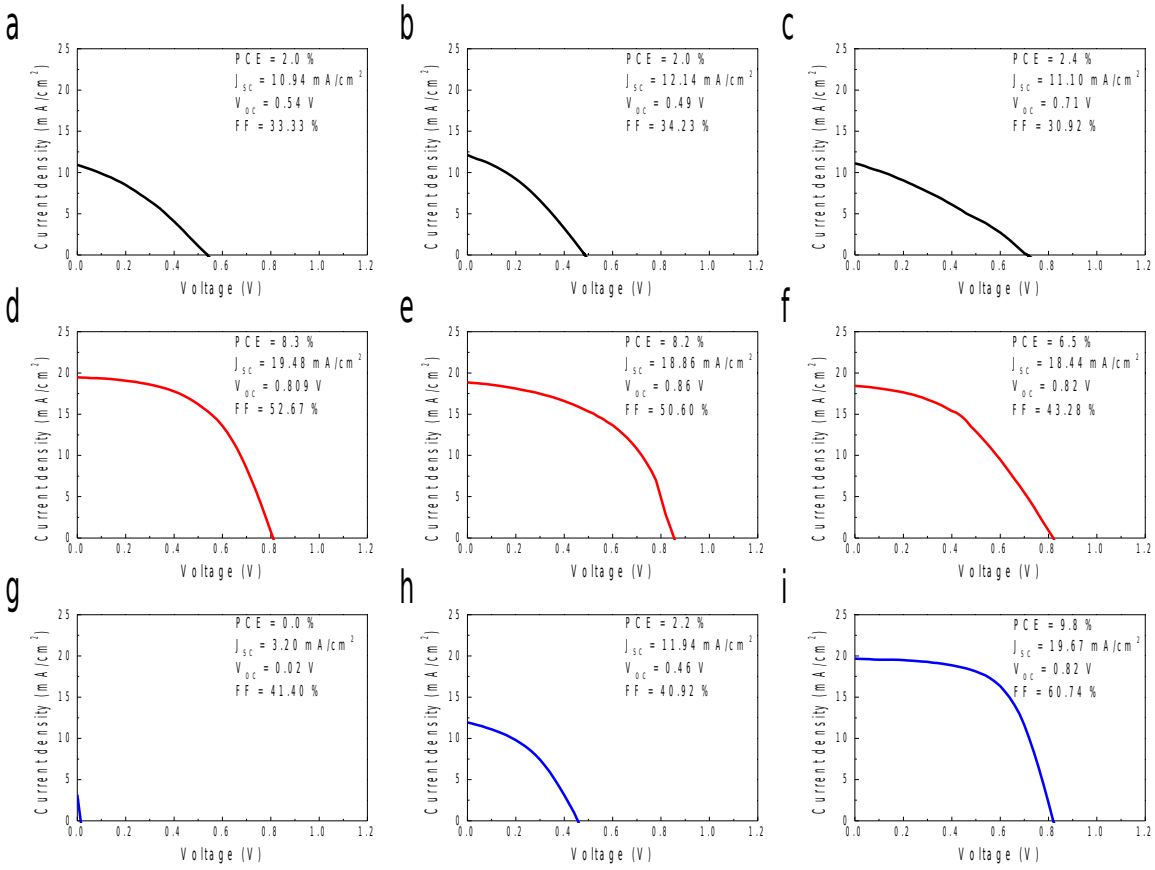

Figure S16. $MAPbI_3$ device performances after different annealing times. a-c, PbI_2-route with **a** 10s, **b** 30s and **c** 300s annealing time; **d-f**, $PbAc_2$-route with **d** 10s, **e** 30s and **f** 300s annealing time; and **g-i**, $PbCl_2$-route with **g** 1800s, **h** 2700s and **i** 3600s annealing time at 110ºC in ambient condition.

References

[1] A. A. Petrov, I. P. Sokolova, N. A. Belich, G. S. Peters, P. V. Dorovatovskii, Y. V. Zubavichus, V. N. Khrustalev, A. V. Petrov, M. Grätzel, E. A. Goodilin, A. B. Tarasov, *J. Phys. Chem. C* **2017**, *121*, 20739.